Chapter 2
Pinning-Engineered $YBa_2Cu_3O_x$ Thin Films

Paolo Mele, Adrian Crisan and Malik I. Adam

2.1 Introduction

In order to be used for practical applications such as lossless current transportation, winding of magnets, etc., superconducting materials should possess not only high enough critical temperature T_c, but also critical current density J_c, and upper critical field B_{c2} as large as possible to cover a wide range of the currently available and future technologies of superconductivity.

Introduction of nanosized artificial pinning centers (APCs) was widely used to strongly enhance J_c of high-temperature superconductor (HTSC) like $YBa_2Cu_3O_x$ (YBCO, $T_c = 92$ K) in magnetic field. Figure 2.1 shows the performance of state-of-the-art YBCO thin films with APCs in comparison with other superconducting materials [1]. It is worth noting the outstanding performance of APCs-added YBCO films at 77 K, surpassing the conventional superconducting metallic cables (NbTi, Nb_3Sn) at 4.2 K. The incorporation of one-dimensional defects such as nanorods in YBCO films prepared by pulsed laser deposition (PLD) could be exemplified as to how effective the APC technology evolves. After the pioneering work of J. McManus-Driscoll and coworkers on YBCO+BZO nanorods [2], in 2008 YBCO films added with 4 wt% BSO have been reported to

P. Mele (✉)
Research Center for Environmentally Friendly Materials Engineering, Muroran Institute of Technology, Muroran, Hokkaido, Japan
e-mail: pmele@mmm.muroran-it.ac.jp

A. Crisan
National Institute of Materials Physics, 077125 Bucharest, Magurele, Romania
e-mail: adrian.crisan@infim.ro; acrisan652@gmail.com

M.I. Adam
Department of Mechanical Engineering, University Tenaga Nasional, Kajang, Malaysia
e-mail: idriesm@uniten.edu.my; omavis1@gmail.com

A. Crisan (ed.), *Vortices and Nanostructured Superconductors*, Springer Series in Materials Science 261, DOI 10.1007/978-3-319-59355-5_2

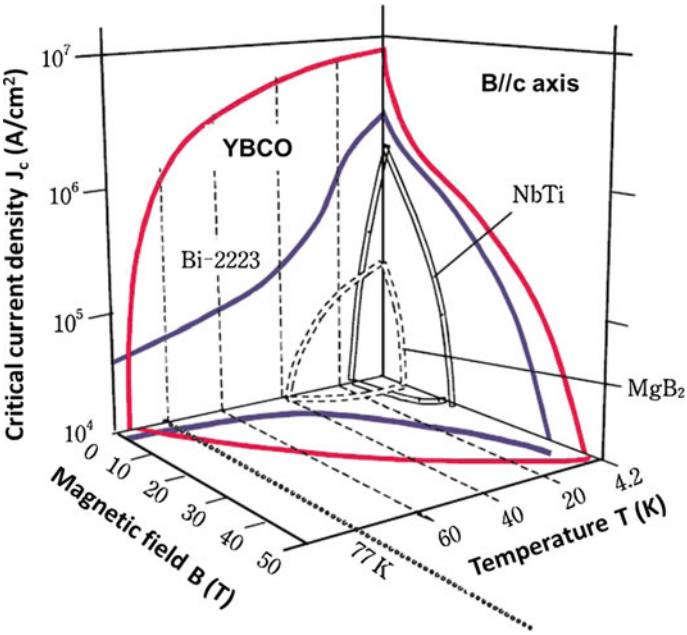

Fig. 2.1 Dependence of critical current density (J_c) on external magnetic field (B) and temperature (T) for various superconducting wires: NbTi (white line), MgB_2 (*white dotted line*), Bi-2223 (*blue solid line*), YBCO (*red solid line*). In the YBCO case, the maximum of the critical current density can be obtained in a wide region. (Reproduced with permission from [1] with slight modification)

generate a $J_c = 0.3$ MA/cm^2 and global pinning force $F_p = J_c \times B = 28.3$ GN/m^3 at 77 K, 3 T (B //c) [3]. Rapid progress in the maximum global pinning force in YBCO added with nanorods has been reported during the following years by decreasing the operating temperature: 120 GN/m^3 at 65 K with niobate addition [4]; 405 GN/m^3 at 40 K in YBCO added with BHO [5]; 700 GN/m^3 at 30 K, 1000 GN/m^3 at 20 K [6]; and even 1750 GN/m^3 at 4.2 K [7] in YBCO with 25% of Zr. Besides F_p^{max}, another parameter used to quantify the applicability range of YBCO films is the irreversibility field (B_{irr}). Remarkable improvements of B_{irr} (77 K) = 11 T of YBCO+BSO have been published recently. $B_{irr} = 14.8$ T (77 K) for MOCVD (Y,Gd)BCO doped with 15% vol Zr [7], $B_{irr} = 15$ T for LTG-SmBCO-BHO [8], and $B_{irr} = 15.8$ T for GdBCO-BHO on Hastelloy [9].

The impressive performances of YBCO added with nanorods are counterbalanced by the fact that J_c is found to be intrinsically anisotropic in relation to the direction of the applied magnetic field with a broad maximum for B//c-axis direction. Current flow anisotropy was identified as one of the critical issues facing the practical applicability of these materials since the value of J_c in certain applications might be needed to be constant in all directions of the applied magnetic field during machine operation. T. Haugan and coauthors opened the way to solve this

issue with their seminal work on Y-211 randomly dispersed particles (3D-APCs) added to YBCO films [10]. After that, big progress has been achieved in YBCO added with isotropic APCs. Impressively, YBCO added with Y_2O_3 nanoislands showed extremely high global pinning force: $F_p > 1TN/m^3$ at 4.2 K [11].

Besides the "basic" one-dimensional and three-dimensional APCs (two-dimensional APCs have been found to be much more difficult to be established), the pinning landscape became extremely rich, thanks to the nanoengineering approach of many groups worldwide in the past decade. Several combinations of APCs have been tried, such as adding randomly dispersed islands to the nanorods, cutting the nanorods when nanolayers are deposited parallel to the films' thickness, and several more diverse approaches. All of them will be covered in this extensive review.

This chapter is divided in three parts:

(i) Critical current and pinning force in pure YBCO superconductors and their limits
(ii) Artificial pinning center approach with broad overview of experimental results and theoretical models
(iii) Summary of the performance of APCs-added YBCO and general conclusion.

2.2 Critical Current and Pinning Force in Pure $YBa_2Cu_3O_x$ Thin Films

After the discovery of YBCO in 1987 [12], the first oxide superconductor with $T_c = 92$ K, a temperature that is larger than the boiling point of nitrogen, the great potential of this material for practical application has been immediately anticipated and many research groups have focused on the transport properties of sintered YBCO. Despite of considerably large irreversibility field ($B_{irr} \sim 7$ T at 77 K) in the bulk form of the sintered material, the critical current was found to have very low values in excess of 10^2 A/cm^2 or so, not surpassing the typical performance of copper cables.

The reason of the low values of J_c has been found into the low coherence length of YBCO, so that consequently J_c does not pass easily through the grain boundaries [13]. Early studies of bulk YBCO and related REBCO (RE = lanthanide rare earth) materials have been demonstrated that J_c can be enhanced thanks to the alignment of the grains by melt-texturing-growth (MTG) approach [14]. MTG allowed obtaining J_c in the order of 10^4 A/cm^2, two orders of magnitude larger than for sintered material. Indeed, the MTG REBCO materials are able to trap huge values of magnetic field [15, 16] and can be used for energy storage. However, as a matter of fact, MTG bulk materials are inherently brittle and then not feasible for development of long and flexible cables for the effective transportation of electrical current.

The same problem of low critical currents due to the misorientation of the grains has been found at first in the so-called first-generation wires and tapes (1G-WT), based on $(Bi,Pb)_2Sr_2Ca_2Cu_3O_x$ (Bi-2223) materials and produced by powder-in tube approach. Bi-2223 tapes can be used for power cables, but are not feasible for use at 77 K in any magnetic field of significant magnitude. The reason is the drastic suppression of B_{irr} (T) to the very low value of 0.2 T due to the large anisotropy [17].

From early 1990s, researchers focused on the development of "second-generation wires and tapes" (2G-WT). 2G-WT are called "coated conductors" (CC): The superconducting layer (usually YBCO or REBCO) is coated on a substrate in such a way as to obtain both in-plane and out-of-plane texturing of the superconducting grains in a biaxial alignment [18]. The biaxial alignment (i.e., the perfect epitaxy) can be easily obtained on a single crystal, which sizes are few cm, but is more difficult to achieve over long lengths (on the km scale) which are indispensable for practical applications.

Two kinds of approaches to prepare long-length CC have been proposed: ion beam-assisted deposition (IBAD) [19] and rolling-assisted biaxially textured substrates (RABiTS) [20]. IBAD technique involves the deposition of biaxially oriented buffer layer on polycrystalline metallic substrate, followed by deposition of superconducting film. In RABiTS, the metallic substrate (Ni) is biaxially textured as effect of cold rolling and recrystallization. The story of 2G-WT is the story of technological progress on IBAD and RABiTS, with continuous improvement in performance (critical current and pinning force) and length of the tapes. However, further discussion on 2G-WT is beyond the scope of this chapter. Nevertheless, the interested reader is kindly referred to the detailed analysis of the 2G-WT which can be found in the excellent textbook [21] and reviews [22, 23].

Parallel to the development of IBAD and RABiTS, a plethora of research has been done and duly published on the fabrication and characterization of YBCO films on single crystals, and the state-of-the-art advancement was the $J_c > 10^6$ A/cm^2 (self-field, 77 K, $B//c$) for YBCO films. It was concluded from this striking development that YBCO films can carry currents two orders of magnitude larger than the MTG YBCO materials.

It is quite impressive to see how, in about 28 years, four orders of magnitude improvement on the value of the critical current in YBCO materials has been achieved, thanks to the combined progress in material and flux pinning engineering.

The epitaxial YBCO films formed on single-crystal substrates via the non-equilibrium process such as pulsed laser deposition (PLD) [24] or chemical routes such as trifluoroacetate-metal oxide deposition (TFA-MOD) [25] and metal organic chemical vapor deposition (MOCVD) [26] have high J_c of 1–5 MA/cm^2 at 77 K and zero field (see, e.g., [27] and references therein, [28]). This is because the various crystal defects which are naturally formed during the deposition of the epitaxial YBCO films such as antiphase boundaries, grain boundaries, stacking faults [29–33], voids, compositional impurities, fine precipitates, and dislocations [34] exist in a high density in the film, in addition to oxygen vacancies and twins

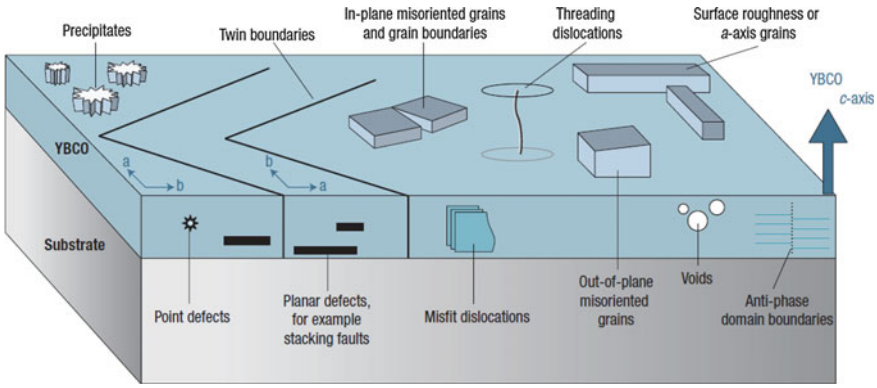

Fig. 2.2 Schematic representation of natural thin-films defects proposed as flux pinning sites in YBCO. (Reproduced with permission from [38])

[35–37]. Schematic representation of natural defects in YBCO thin films is reported in Fig. 2.2 [38].

From early studies of PLD-prepared YBCO superconductor films, it has been proven that the three-dimensional Volmer–Weber growth mechanism creates steps on crystal substrate which acts as nucleation sites thereafter [27]. AFM images show growth spirals on PLD film, and this feature was accepted as clear evidence for the presence of screw dislocations in the structure of the grown films. Furthermore, cross-sectional TEM images have also presented evidence of the columnar microstructure of the PLD films. This was ascribed to the growth of spiral columns intertwined with the grain boundaries. The dislocations, both screw and edge dislocations which are found to extend along the *c*-axis of the films, have been suggested to act as strong pinning centers for the vortices in YBCO films. This was the case since the dislocation core is normal and its diameter is about 1–3 nm, which is comparable with the coherence length of the superconductor [30–40]. However, it is very difficult to control the density and distribution of the dislocations in order to improve J_c under magnetic fields. This has been the problem for improving the in-field J_c of the pure YBCO films for a long period of time.

2.3 Critical Current and Pinning Force in $YBa_2Cu_3O_x$ Thin Films with Artificial Pinning Centers (APCs)

Based on the Ginzburg–Landau model [41, 42], insertion of additional artificial pinning centers (APCs) on the nanoscale-prepared films is found to be useful as well as effective approach in enhancing the dynamic J_c in the complex structure of these materials. The added defects were found to prevent the movement of vortices. According to global pinning theory, any non-superconducting region of a size *d* that

is equivalent to few nanometers or approximately equal to the size of a vortex core radius can act as APC. Hence, the pinning energy of the vortex is then given by

$$u_P = \frac{B_c^2}{2\mu_0}\pi\xi_{GL}^2 d \tag{2.1}$$

where B_c is the thermodynamically critical field, and ξ_{GL} is the Ginzburg–Landau coherence length. The elementary pinning force, i.e., the pinning force associated with one single vortex pinned by one single particle can be written as

$$f_p = U_p / \xi_{GL} = \frac{B_c^2}{2\mu_0}\pi\xi_{GL} d \tag{2.2}$$

The global pinning force $F_P = J_c \times B$ therefore is directly proportional to the number of particles N so that the critical current is expressed by

$$J_c = \frac{F_P}{B} = \frac{Nf_p}{B} = \frac{NB_c^2}{2\mu_0 B}\pi\xi_{GL} d \tag{2.3}$$

A classical representation of (2.2) and (2.3) is used for the analysis of an YBCO MTG bulk containing round-shaped Y_2BaCuO_5 (Y211) nanosized particles having a density N_p and lattice spacing a_f, where $1/N_p = a_f^2\sqrt{3}/2$ and size d. In this case, the critical current density of the system is calculated as

$$J_c = \frac{\pi\xi_{GL}B_c^2}{2\mu_0 B\sqrt{\phi_0}}\frac{N_p d^2}{\sqrt{B}}\left(1 - \frac{B}{B_{c2}}\right) \tag{2.4}$$

It can be seen from the above equation that the J_c of the system is directly proportional to the volume fraction of the nanoparticles, $N_p d^3$, divided by the size of the vortex core d or, in other words, the number of YBCO/Y211 interfaces. By extension, this theoretical approach led the experimentalists to choose an approach allowing the reduction of the size d of the Y211 inclusions in the films in order to increase J_c. The refinement of Y211 nanoparticle size and the consequent improvement of J_c have been successfully accomplished by addition of secondary phases (e.g., Pt [14]).

The APC approach has been successfully extended to YBCO and REBCO thin films, and outstanding results, with global pinning force exceeding 30 GN/m^3 at 77 K, have been obtained by many groups all over the world in the past 10 years. Summary of pinning performance at 77 K is given in Fig. 2.3.

In the last 2 or 3 years, several groups focused their investigations on the lower temperatures (from 30 K down to 4.2 K) and high magnetic fields (from 10 T up to 30 T). The performance of APCs-added YBCO and REBCO overcame the "psychological threshold" of 1000 GN/m^3, with the present record value of 1750 GN/m^3 at 4.2 K, 30 T for YBCO+15%Zr prepared by MOCVD: 100-fold than the

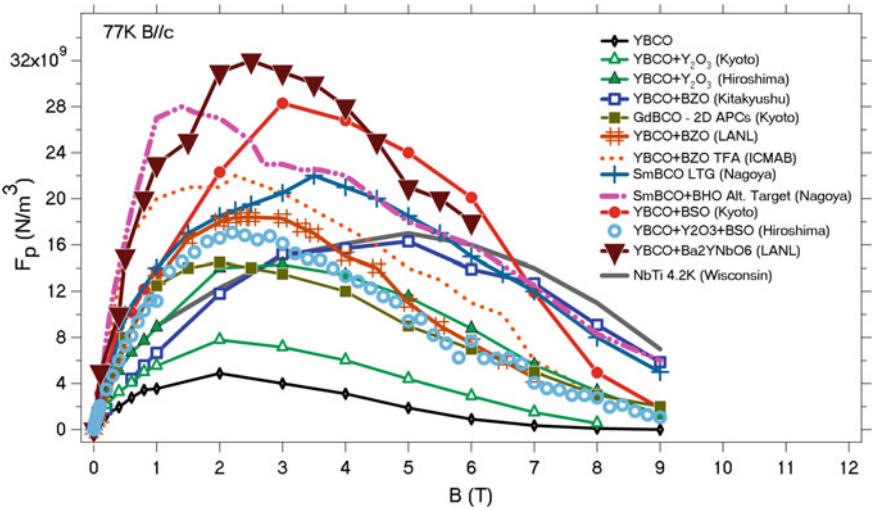

Fig. 2.3 The global pinning force F_p drawn against the applied magnetic field B at (77 K, $B//c$) for YBCO films with several types of APCs. Majority of the samples are described in the main text. The F_p performance of NbTi wire at 4.2 K was included as a milestone

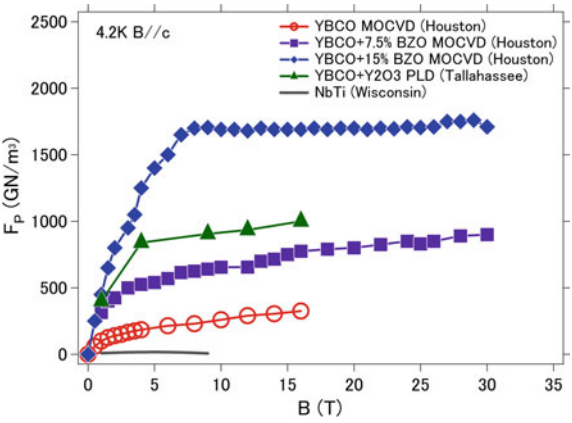

Fig. 2.4 The global pinning force F_p drawn against the applied magnetic field B at (4.2 K, $B//c$) for YBCO films and tapes with several types of APCs. The samples are described in the main text

maximum pinning force of NbTi at the same temperature [7]. Summary of pinning performance at 4.2 K is given in Fig. 2.4.

The broad-spectrum strategies so far implemented for the production of superconducting thin films doped with different APCs can be classified into three main stream steps. The preliminary step is directed toward finding an element, elemental oxide, or elemental compound with feasible APC features. The second step is rather practical and is concentrated onto how to incorporate the viably defined APCs into YBCO or REBCO superconducting matrix so that the immediate objective here is to provide a potential pinning site. The third and final broad strategy was devoted to

the ways and means that could possibly lead to practical control of the spacing and the spatial distribution of APCs in the superconducting matrix so that a clear correlation between APCs and the output values of J_c and F_p can be realized.

The APC selection is usually based on empirical trials and can also be predicted theoretically or in some cases through the combination of the two. While the analysis of J_c and F_p can be done through modeling of simple empirical equations, the Ginzburg–Landau theory of superconductivity stood out as best theoretical background that is extensively used for data analysis. Different examples of APC engineering approaches for YBCO thin films will be given in the subsequent pages.

One of the most common classifications of the APCs is related to their dimensionality and shape in relation to the superconducting matrix. Four kinds of APC can be distinguished as follows:

(i) Zero-dimensional APCs (0D-APCs): the defects smaller than ξ, such as vacancies, cation disorder, or atomic substitutions at Y or RE site
(ii) one-dimensional APCs (1D-APCs), i.e., linear defects: linear dislocations obtained by decoration of the substrate; columnar defects obtained by heavy ion irradiation; and columnar defects incorporated by the addition of secondary phases such as dislocations and columnar defects
(iii) two-dimensional APCs (2D-APCs), i.e., planar defects such as interfaces in multilayers, small-angle grain boundaries, antiphase boundaries, and surfaces of large precipitates
(iv) Three-dimensional APCs (3D-APCs) such as nanoparticles and secondary phases of the scale of ξ or more.

Other four subcategories are generally obtained by the combination or modification of the aforementioned main types which include:

(v) Segmented 1D-APCs, obtained by alternating layers with pure YBCO and layers of YBCO+nanocolumns
(vi) Mixed 1D+3D APCs, obtained by simultaneous combination of columnar defects and nanoparticles in hybrid films
(vii) Multilayered 1D+3D-APCs obtained by alternating columnar defects and nanoparticles in multilayers
(viii) Combined multilayers and nanorods, obtained by simultaneous incorporation of APCs engineered parallel and perpendicular to the *c*-axis of the film.

Figure 2.5 represents the four basic cases and their most common combinations.

2.3.1 Zero-Dimensional APCs (0D-APCs)

0D-APCs (or dilute doping, or minute doping) of YBCO or REBCO thin films is referred to the substitution of very small amounts of foreign elements at Y or RE site. Several substitutions by element M (M = Tb, Ce, Pr, Nd, La, Co, and Eu) at

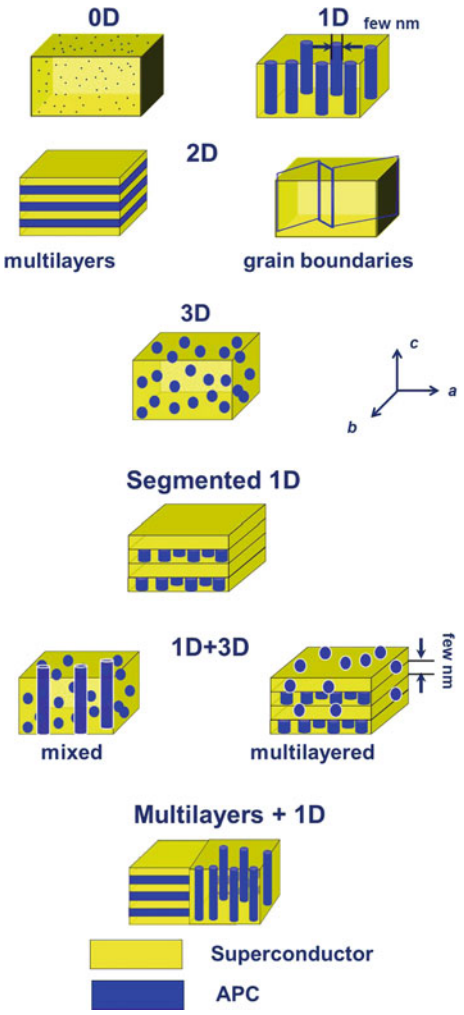

Fig. 2.5 Schematic representation of nanometric artificial pinning centers (APCs) of different dimensionality incorporated in YBCO superconducting thin film. Details are given in the main text

the Y site of YBCO and RE site of REBCO (RE = Dy) were studied [43–48]. The doping enhances J_c and F_p over the range of the applied magnetic fields, and this is attributed to two intertwinned factors. Firstly, there is the enhanced concentration of nanoprecipitates of these substituents in YBCO film compared to the case of the pure YBCO one (see Fig. 2.6a). Consequently, the resulting stress field induces lattice misfit in the final structure of the hybrid film. In the case of YBCO added with Eu at Y site, the most consistent self-field transport J_c values were achieved for Y/Eu = 0.7/0.3 films, with arguably the densest and smoothest microstructures (Fig. 2.6b).

Advanced doping with three different rare earth elements at RE site was tried in the middle of 1990s in melt-textured $(Nd_{0.33}Eu_{0.33}Gd_{0.33})Ba_2Cu_3O_x$ (NEG-123)

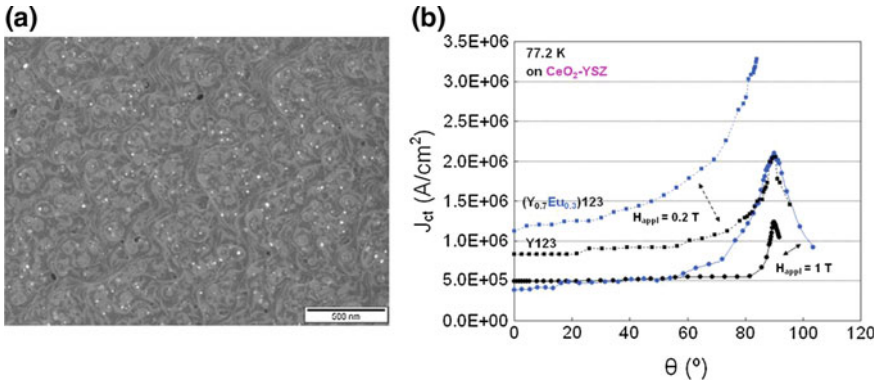

Fig. 2.6 **a** SEM micrograph showing nanoprecipitates on the surface of $(Y_{0.7}Eu_{0.3})Ba_2Cu_3O_y$ film grown on CeO_2–YSZ substrate; **b** J_c (77.2 K) of $(Y_{0.7}Eu_{0.3})Ba_2Cu_3O$ and YBCO films on CeO_2–YSZ substrates, for varying angle and $H_{appl} = 0.2$ and 1 T; $\theta = 0°$ corresponds to $H//c$, and $\theta = 90°$ is for $H//ab$. (Both panels reproduced with permission from [44])

and has shown marvelous performances in terms of J_c and irreversibility field [49, 50]. In the bulk form of these materials, the self-field J_c at 77 K has reached the level of 10^5 A/cm^2 ($H//c$-axis), and the irreversibility field was recorded ~15 T when the measurement was performed at the applied field of 5 T. A very important as well as intuitive aspect deduced from the early results is the possibility to reduce the pinning defect size down to nanoscale level and to engineer a method that brings the defect size close to the coherence length. These nanoscale particles of secondary phases, Zn, Mo, Ti, Nb, etc., have eventually enhanced the flux pinning of these materials up to 3 times compared to that measured on pristine YBCO compounds. As a result, the pinning force density remained strong up to the liquid oxygen temperature (90.2 K), which enables magnetic levitation near to the vicinity of critical temperature of YBCO [51]. The applicability of levitation technology is thus extended by about 13 K above the usual limit of the boiling point of liquid nitrogen.

Along this line, studies on NEG-123 films were tried with emphasis on the great potential of this material for practical applications [52–54]. In comparison with GdBCO films, pinning performance and irreversibility field were enhanced. It appeared, however, that there is not much difference between the J_c and F_p values of the NEG-123 films and the bulk form of the same material. This fact may be related to issues regarding the structural optimization.

2.3.2 One-Dimensional APCs (1D-APCs)

In the attempt to improve J_c over a wide range of magnetic fields and field orientations, the one-dimensional artificial pinning centers (1D-APCs) in the form of

columnar defects, screw and edge dislocations, and their consequential lattice strain constitute the most investigated type of pinning centers associated with films and coated conductors alike. This type of pinning centers is generally classified into three subcategories.

The first category comprises columnar defects that are introduced into the film by heavy ion and/or neutron irradiation.

The second subtype is the linear dislocations which can be obtained by decoration of substrate prior to the thin-film deposition.

Nanocolumns composed of secondary non-superconducting phases incorporated in superconducting film encompass the third subtype: the 1D nanorods. The ability of these 1D nanorods in restraining the vortex flux line mobility and, hence, the dramatic improvement of J_c and the global flux pinning F_p were clearly demonstrated in the optimally doped $BaMO_3$–YBCO samples with (M = Zr, and Sn) [3]. A comparison of the F_p values of the two samples, however, showed that the global pinning is larger in the $BaSnO_3$-doped sample. Additions of other perovskite ($BaHfO_3$) or double perovskite nanorods were tried as well.

2.3.2.1 Columnar Defects by Neutron and Ion Irradiation

In the first half of 1990s, significant efforts have been made to create non-superconducting columns by high-energy irradiation of YBCO single crystals or thin films with neutrons and heavy ions [55–59]. Both neutrons and heavy ions have been found as efficient tools for improving J_c, F_p, B_{irr} of the thin films since the size of defects and vortex core is comparable. Furthermore, the size, density, and shape of defects are controllable though variation of energy and fluence of the ions or neutrons.

Due to the high cost of irradiation, this top-down approach was confined to small-size samples and laboratory studies for long time. Very recently [60], development of reel-to-reel neutron irradiation facility drastically lowered the cost to few USD/m so that this way appears feasible for large-scale applications. In the framework of this "revival," fast irradiation (exposure of just one second per 0.8 cm^2) by 3.5 meV oxygen ions significantly improves the in-field performance of YBCO tapes without modification of the coating conductor growth in the industrial process [61].

Develos-Bagarinao et al. [62] proposed a cost-effective way to create nanopores in MOD YBCO films: conventional Ar ion milling of the films through nanoporous anodic aluminum oxide (AAO) templates. After irradiation, etching of the YBCO film revealed columnar voids deeply penetrating into YBCO matrix (Fig. 2.7a). Despite to low pore density (~4.56 μm^{-2}), in-field J_c (2 T) was enhanced by a factor of two with respect to the J_c of the unirradiated films, with typical *ab*-pinning (Fig. 2.7b). With AAO membranes having much higher density of pores, *c*-axis-correlated pinning and much higher J_c are expected.

Another original approach has been proposed by Sueyoshi et al. [63] by investigating the flux pinning property in a GdBCO-coated conductor splayed with

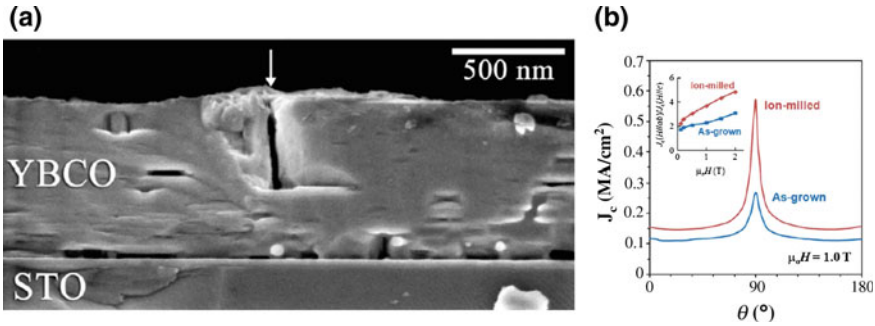

Fig. 2.7 **a** Cross-sectional SEM image of an Ar ion-milled, Br-ethanol chemically etched YBCO film. The arrow indicates a typical columnar void created by the ion milling and subsequent etching (reproduced with permission). **b** In-field current-carrying performance and structural properties comparing as-grown to ion-milled YBCO films: Angle-dependent J_c (θ) at 77.3 K, 1 T of as-grown YBCO and ion-milled YBCO. The inset shows the ratio $J_c(B//ab)/J_c(B//c)$ as a function of applied field. (Both panels reproduced with permission and slightly modified from [62])

Xe^+ ions where the resulted columnar defects were oriented parallel to both *c*-axis and the *ab* plane. The angular dependence of $J_c(\theta)$ has been shown to produce multiple maxima in the field angular orientation dependence of the critical current.

2.3.2.2 Linear APCs in YBCO Films Deposited on Decorated Substrates and on Functional Buffers

The first bottom-up approach to produce 1D-APCs was the deposition of nanodots on the substrates followed by deposition of the superconducting film. The immediate effect of the decoration of substrates by 1D-APCs is the formation of linear dislocations parallel to the *c*-axis of the superconducting film. This procedure is now usually named "substrate decoration method."

In the pioneering work of Crisan et al. [64–66], they deposited an amorphous phase of Tl-based thin-film superconductor on substrates decorated by sputtered Ag nanodots. This approach was successful, and the J_c was enhanced to a value more than one order of magnitude (Fig. 2.8). The drawback of Tl-based materials lies in their unsuitability for applications because of the toxicity of Tl. Later on, the technology was applied to YBCO films, numerous studies on improvement of J_c by linear defects induced by decoration were published so far, and several decoration techniques were subsequently employed. Examples are annealed CeO_2 buffer for YBCO films [67, 68], iridium-sputtered particles for YBCO films [69], Au, Ag, and Pd PLD-deposited nanodots [70, 71], spin-coated $BaTiO_3$ and $BaZrO_3$ nanoparticles [72], gas-phase-deposited Y_2O_3 particles [73], and PLD-deposited Y_2O_3 particles [74].

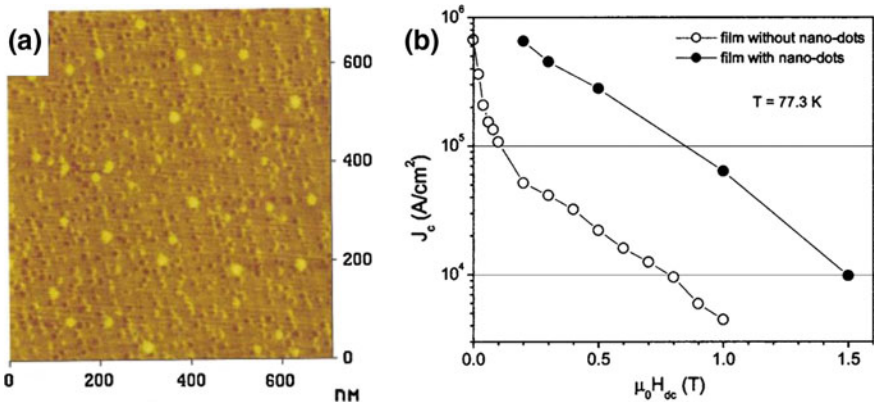

Fig. 2.8 **a** Atomic force micrograph of Ag islands grown on annealed $SrTiO_3$ (100) by 5 s rf sputtering; **b** Critical current density of (Cu, Tl)$BaSrCa_2Cu_3O_y$ films grown on substrate without (*empty symbols*) and with (*filled symbols*) Ag nanodots at 77 K and various dc fields, estimated from Brandt's formula. (Both panels reproduced with permission from [64])

K. Matsumoto et al. proposed the formation of distributed nanosized Y_2O_3 islands on the substrate surface, followed by YBCO [75–80] or SmBCO [81] deposition. Depending on deposition conditions, the formation of yttria nanoislands of diameter 15–50 nm and height 4–10 nm was found to require a small number of laser shots, typically 5–10. After chemically etching deposited YBCO films, the density of the etch pits and the distance between closest neighbors are nearly identical to those observed for the nanoislands. Nanoislands induce the formation of extended linear defects such as dislocations, and nearly, all the islands can induce dislocations inside the film. In such a way, the density of dislocations was enhanced up to 200–220/μm^2—about three times larger than the natural dislocation density values. In the best conditions (substrate decorated with 10 laser pulses on Y_2O_3 target), both J_c and the maximum global pinning force of the samples at 77 K were enhanced by up to 1.7 times than those of pure YBCO film deposited in the same conditions, and clear *c*-axis-correlated pinning was observed.

Although the fabrication of PLD film on the decorated substrate results in an enhancement of J_c in magnetic field, the decoration technique is very laborious and delicate process. The growth window for deposition is very narrow where a small difference in the number of the laser shots can radically change the size and distribution of the nanoislands in the film.

More recently, Tsai and coworkers deposited YBCO films by PLD on STO substrates buffered with $(Fe_2O_3)_x(CeO_2)_{1-x}$ functional ferromagnetic composite [82]. The Fe_2O_3 vertically aligned nanopillars (VAN) embedded in CeO_2 matrix provide significant increase in the J_c (Fig. 2.9) due to pronounced magnetic pinning effect. The amount of nanopillars can be tuned by varying the concentration x of Fe_2O_3 in the matrix. Best result was obtained when $x = 0.3$: F_p^{max} (65 K) ~ 20 GN/m^3, F_p^{max} (40 K) ~ 180 GN/m^3, and F_p^{max} (5 K) ~ 1100 GN/m^3.

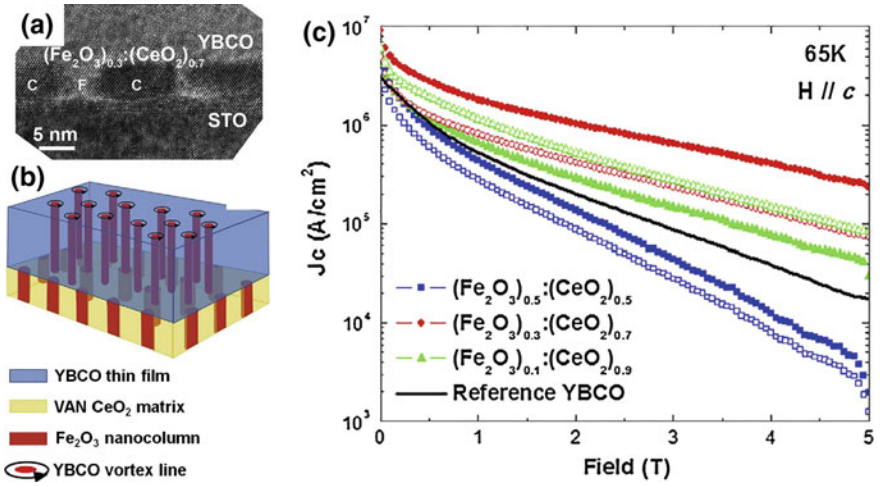

Fig. 2.9 **a** Cross-sectional high-resolution TEM micrographs and **b** illustration of pinning landscape of $(Fe_2O_3)_{0.3}$:$(CeO_2)_{0.7}$ buffer containing vertically aligned nanopillars (VAN) below YBCO film. **c** In-field performance ($J_c(B//c)$) as a function of applied magnetic field plots of the VAN nanolayers doped samples compared with the reference YBCO sample measured at 65 K. (All panels reproduced with permission and slightly modified from [82])

2.3.2.3 Oxide Nanocolumns Embedded in Superconducting Films

The majority of published reports on 1D-APCs is devoted to the formation and characterization of self-aligned nanorods of 5–15 nm diameter grown in the epitaxial YBCO films by ablation of YBCO target doped with a small wt% of perovskites $BaMO_3$ (BMO, M = Zr, Sn, Hf) by PLD or MOCVD methods [2–4, 83–128].

A key question related to columnar 1D-APCs is: Why perovskites (BMO) form nanorods in YBCO while other dopants (Y_2O_3 for example) do not? This question remained unanswered for several years. Wu et al. [129–134] recently proposed an explanation based on the interfacial strain (Fig. 2.10).

(i) the *local* YBCO/dopant interfacial strain, extended for few nm around the dopant, determines the morphology of the nanostructures (vertical alignment = nanorods) or horizontal alignment (particles or nanopatches) inside the films (Fig. 2.10a);

(ii) the *global* film (YBCO+incorporated dopants)/substrate interfacial strain, extended for hundreds of nm, tunes the 1D-APC landscape: Nanorod orientation evolves as *c*-aligned → splayed → *ab*-aligned (i.e., nanopatches or nanolayers) as the global strain increases. It is worth noting that if the global strain is negligible, nanorods remain parallel to the *c*-axis up to very high concentrations of the dopant (up to 45 vol.%) (Fig. 2.10b).

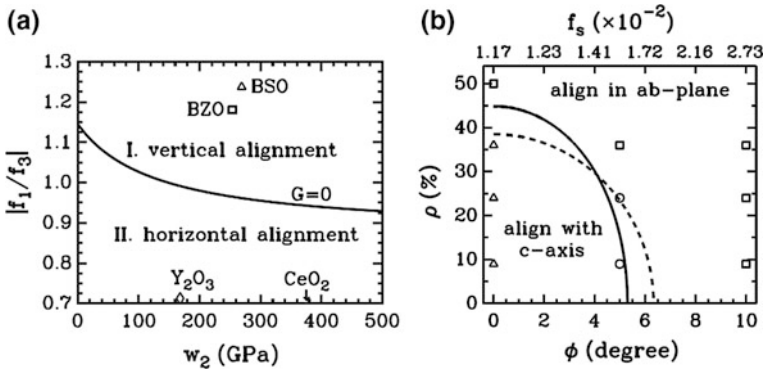

Fig. 2.10 **a** Threshold of f_1/f_3 as a function of w_2 for nanodefects (BZO, BSO, Y_2O_3, CeO_2) orientation in the *c*-oriented YBCO film on lattice-matched substrates, where f_1 and f_3 are the lattice mismatch between the film and dopant in the [100] and [001] directions, respectively, and w_2 is a function of the elastic constants of the dopant. Below (above) the *solid curve*, the vertical (horizontal) alignment is unattainable (Reproduced with permission from [125]). **b** Phase diagram for BZO nanostructure in *c*-axis-oriented YBCO films, where $r(\%)$ is the volume density of BZO in the film, f is the vicinal angle of STO substrate, and f_s is the substrate/film lattice mismatch. The solid curve is the calculated phase boundary. Experimental points are indicated by *triangles* (*c*-axis-aligned nanorods), *squares* (*ab* plane-aligned nanopatches and circles (mixed nanorods and nanopatches). (Reproduced with permission from [87])

Additionally, in [132–134], Wu and coworkers applied an elastic strain model to understand the effect of the lattice strain on the diameter of the BZO nanorods embedded in YBCO films. They found that the radius R of the nanorods was not dramatically affected by the concentration of BZO in the targets and is varying only slightly in the range $\chi = 0.2 \sim 0.7$, where $\chi = R/D$, the ratio between radius of the nanorods (R), and distance between two adjacent nanorods (D). R can be predicted from c and E_{elastic} of the nanorods according to the relation

$$R = \frac{\gamma_S \chi^2}{\gamma_0 + \gamma_1 \chi^2 - E_{elastic}} \tag{2.5}$$

where $\gamma_s = C_s \varepsilon_{rod}$, $\gamma_0 = C_0 \varepsilon_{rod,}$ and $\gamma_1 = C_0 \varepsilon_{rod}$; C_s, $C_{0,}$ and C_1 are constants, while ε_{rod}, the elastic energy of the nanorods, is calculated from the elastic constants c_{ij} of BZO and YBCO and mismatch between YBCO and the nanorods.

This approach can be extended to YBCO-BSO and YBCO-BHO [134]. Figure 2.11 shows as individual points the experimental values of R as reported from several groups and our predicted value of R for the three systems YBCO-BZO, YBCO-BSO, and YBCO-BHO using different values of the constants. It appears that $R_{BSO} > R_{BZO} > R_{BHO}$. Our results are consistent with [134] even if in such work same value of $\gamma_0 = 180$ is used for the three systems. This suggests a universal behavior for R versus χ. It is quite remarkable that following this approach it

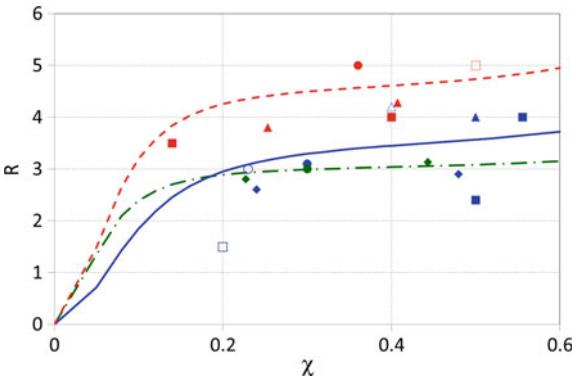

Fig. 2.11 Nanorod radius calculated from (2.5) as a function of χ for BZO (*blue* continuous line), BSO (*red dashed line*), and BHO (*green dashed* and *dotted line*) nanorods in YBCO films, using $C_s = 0.9$, $C_1 = 85$, $C_0 = 275$ for BZO; $C_s = 0.5$, $C_1 = 75$, $C_0 = 316$ for BSO; and $C_s = 0.4$, $C_1 = 100$, $C_0 = 290$ for BHO (see main text for details). Individual points are the measured nanorod radius of BZO in YBCO from [88] (*blue filled squares*), [84] (*blue empty square*), [132] (*blue filled diamond*), [6] (*blue empty diamond*), [111] (*blue filled triangle*), [3] (*blue empty triangle*), and [83] (*blue filled circle*); BSO in YBCO from [117] (*red filled triangles*), [116] (*red filled squares*), [115] (*red empty square*), and [79] (*red filled circle*); BHO in YBCO from [83] (*green filled circle*) and an unpublished work (Mele et al. 2013) (*green filled diamonds*)

is possible to predict the diameter and density of the nanorods (or any other kind of defect) embedded in a film knowing the elastic constants and crystalline parameters of the materials.

Another systematic work comparing the effect of BMO (M = Zr, Sn, Hf) on the superconducting properties of YBCO was recently proposed by Horide et al. [83]. It was shown that only B_Φ (i.e., the density of the nanorods) and not BMO selection nor wt% content are affecting the T_{irr}/T_c curves.

When the nanorods are added to a YBCO film, the maximum pinning force is given for *B*//c direction, and the critical current can be calculated from the solution of the London and Ginzburg–Landau equations for the case of columnar pins [42]:

$$J_c^{columns} = \frac{\Phi_0}{32\pi^2 \xi_{ab} \lambda_{ab}^2} \ln\left(1 + \left(\frac{C_0}{\sqrt{2}\xi_{ab}}\right)^2\right) \tag{2.6}$$

In this expression, C_0 is the radius of the columnar pin, Φ_0 is the flux quanta, $\lambda_{ab} = \lambda_0 (1 - t^4)^{-0.5}$ is the London penetration depth in the *ab* plane, $\xi_{ab} = \xi_0 (1 - t)^{-0.5}$ is the coherence length in the *ab* plane, and *t* is the reduced temperature: $t = T/T_c$. Equation (2.5) is valid when the sizes of defects and the coherence length in the *ab* plane are comparable. In the case of YBCO, $\lambda_0 = 150$ nm and $\xi_0 = 1.5$ nm [17].

$BaZrO_3$ (BZO) Nanocolumns

In the early times (2005), $BaZrO_3$ (BZO) was very popular material to be used as dopant. The first report has been published by McManus-Driscoll et al. [2] and immediately followed by the publication of many more reports in which the likelihood of the new dopant as a good pinning catalyst is revealed [84–100]. The nanorods are found to accumulate longitudinal and parallel to the *c*-axis of the films, and they act as *c*-axis-correlated pinning centers (Fig. 2.12). By utilizing the BZO doping in YBCO films, the J_c was pushed up and eventually reached 0.7 MA/cm^2 (77 K, 1 T, *B*//c) and 0.1 MA/cm^2 (77 K, 5 T, *B*//c). The achieved values correspond to several times J_c of the epitaxial YBCO films. Consequently, the F_p^{max} is increased to reach values of 12–16 GN/m^3 (77 K, *B*//c) which are quite close to those of NbTi (16 GN/m^3, 4.2 K). It was noticed that there is an optimal value in the amount of BZO doping, but the matching field B_ϕ value has also reached 8–10 T. As a result, the B_{irr} curve is greatly pushed up to the high magnetic field side from 5–7 T to 8–11 T at 77 K and *B*//c. Introduction of BZO nanorods by means of mixed target or surface-modified targets was carried out, and similar results were reported for several other REBCO materials with higher T_c than YBCO, such as NdBCO [101–104], ErBCO [105–108], EuBCO [109], and the LTG-SmBCO [110].

In thin films prepared by PLD, the performance of BZO-added YBCO was surpassed by BSO and BHO (see the following paragraphs). Nevertheless, more

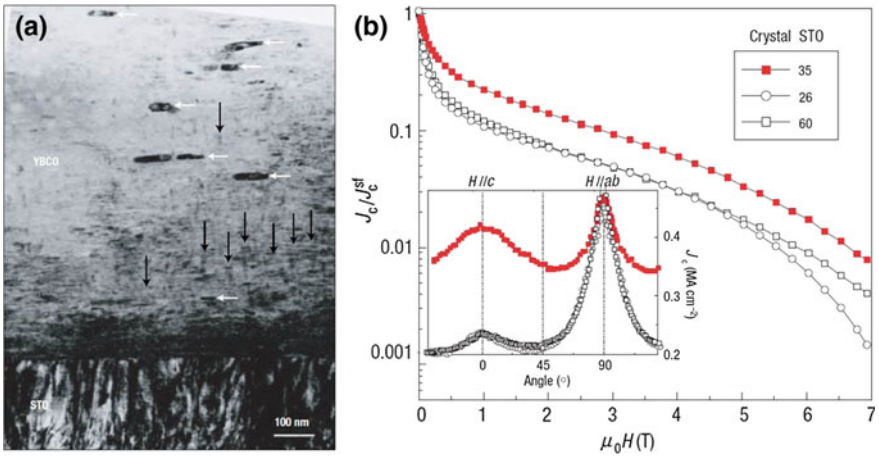

Fig. 2.12 **a** Low-magnification TEM micrograph showing nanoparticles of $BaZrO_3$ in YBCO +$BaZrO_3$ films on STO-buffered MgO single crystals. Some of the nanoparticles have been labeled using white arrows and some of the columnar defects by black arrows; **b** normalized critical current density J_c/J_c (sf) at 75.5 K versus magnetic field applied parallel to the *c*-axis for pure YBCO and YBCO+$BaZrO_3$ films deposited on single-crystal $SrTiO_3$ substrates; inset shows the angular dependence of J_c at 1 T with sample 60 data multiplied by 0.75. Open points are for pure YBCO, and filled points are for YBCO+$BaZrO_3$. (Both panels reproduced with permission from [2])

recently, the group of V. Selvamanickam at Houston University [6, 111–113] reported outstanding results in (Y,Gd)BCO thin films (thickness about 0.9 μm) deposited by MOCVD method, incorporating heavy concentrations of Zr (7.5%, 15%, 25% in volume). In 15% BZO-added (Y, Gd)BCO, the maximum pinning force density F_p^{max} reached 14 GN/m^3 at 5 T, 77 K, which is comparable with F_p^{max} of NbTi at 4.2 K, and the impressive 1.7 TN/m^3 at 4.2 K [6]. Another significant finding is the extremely high B_{irr} at (77 K) ~ 14.8 T, a value that surpasses the B_{irr} ~ 11 T of the NbTi superconductor at 4.2 K [6].

Eventually, thickness of the films was increased up to 2.2 μm with incorporation of BZO nanorods fully extended throughout the whole thickness of the film (Fig. 2.13a), and addition of 20% Zr was recognized [6] as the most effective with critical current of 4206 A/12 mm at 30 K, 2.5 T, corresponding to J_c of about 15 MA/cm^2. This performance exceeds a fourfold improvement in critical current at the operating condition of a 10 MW wind generator (3000 A/12 mm at 30 K, 2.5 T). Indeed, it is a factor of 5.6 higher than the critical current values of commercial coated conductors available today. Linear correlation can be established between J_c (77 K, 3 T, *B*//c) and J_c (*T*, *B*//c) for temperatures lower than 20 K and fields larger than 9 T [112]. Indeed, it has been demonstrated that in these MOCVD-YBCO films highly doped with Zr, the requirement to have J_c of 15 MA/cm^2 at 30 K, 2.5 T (*B*//*c*) is to have a large self-field J_c at 77 K: between 2.5 and 3.8 MA/cm^2 [113]. In the present status, the MOCVD-(Y,Gd)BCO +BZO tapes appear as the most promising material for practical application of the second-generation tapes. Summary of the performances of MOCVD-YBCO-Zr tapes is reported in Fig. 2.13b.

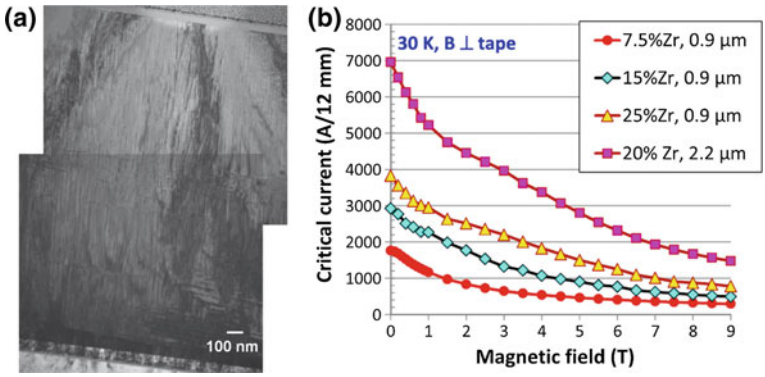

Fig. 2.13 **a** Cross-sectional TEM image of a 2.2-mm-thick 20 mol% Zr-doped (Gd, Y)BaCuO thin film showing well-aligned $BaZrO_3$ nanocolumns throughout the film thickness; **b** magnetic field dependence of critical currents of a 2.2 mm GdBCO tape with 20% mol addition of Zr and the best 0.9-mm-thick GdBCO tapes with 7.5%, 15%, and 25% addition at 30 K in the orientation of filed parallel to the *c*-axis. (Both figures reproduced with permission from [6])

$BaSnO_3$ (BSO) Nanocolumns

The $BaSnO_3$ (BSO) nanocolumns introduced into YBCO were the next try for finding a better nanocomposite superconducting film. Numerous works related to the introduction of the relatively new dopant into YBCO were published in the literature [3, 114–122]. The rather dense and straight in shape BSO nanorods are easily formed in YBCO films. Because the lattice mismatch of BSO compound with YBCO is better than that of the BZO, deterioration of T_c of the films due to the presence of non-superconducting species in the superconducting matrix is moderate. As a result, the YBCO thin films with BSO nanorods are found to have excellent pinning properties.

Historically, first reports on the BSO-added YBCO were published by Varanasi et al. [114–118]. They used a pie-shaped YBCO target, removing a 30° YBCO sector and substituting it with a BSO sector. The periodical ablation in PLD chamber of BSO sector generated BSO nanorods parallel to the *c*-axis of the film (Fig. 2.14a). The angular dependence of J_c shows wide peak with a maximum at *B*//c direction, which is the signature of *c*-axis-correlated pinning (Fig. 2.14b).

The YBCO-BSO system was extensively studied by Mele et al. [117] proposing systematic increment of the BSO content by means of mixed YBCO-BSO targets. Same as in the case of BZO, the perovskite phase is incorporated in the YBCO film with a shape of nanorods, independently from the way used to add the second phase to the target (pie-shaped or mixed).

Figure 2.15 shows the morphology and $F_p(B)$ characteristics of YBCO+BSO films with systematic increment of BSO content. It is clear that concentration and diameter of the nanorods increase with the BSO content in the target. The highest F_p^{max} of the 4wt% BSO-doped YBCO film is 28.3 GN/m^3 (77 K, *B*//c), and it corresponds to about twice as much compared to the BZO-doped films of the same

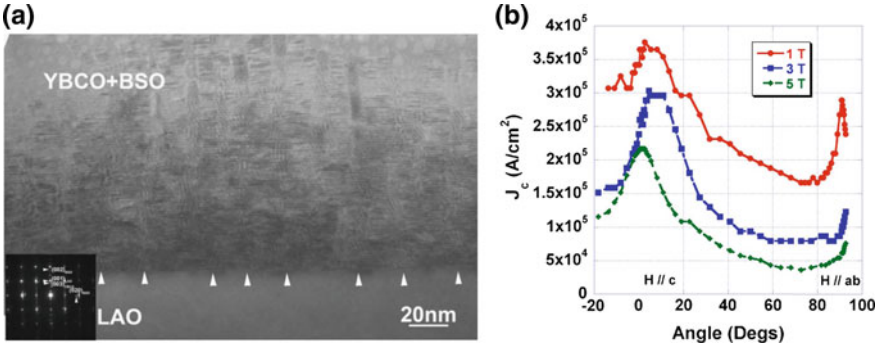

Fig. 2.14 **a** Cross-sectional TEM image of an YBCO+BSO sample on a $LaAlO_3$ substrate. The particles were identified to be $BaSnO_3$ in the selected area diffraction pattern. Nanocolumns extending through the thickness are marked by arrows; **b** angular dependence of J_c values of YBCO+BSO sample on a $LaAlO_3$ substrate at various applied fields of 1, 3, and 5 T at 77 K. (Both figures reproduced with permission from [115])

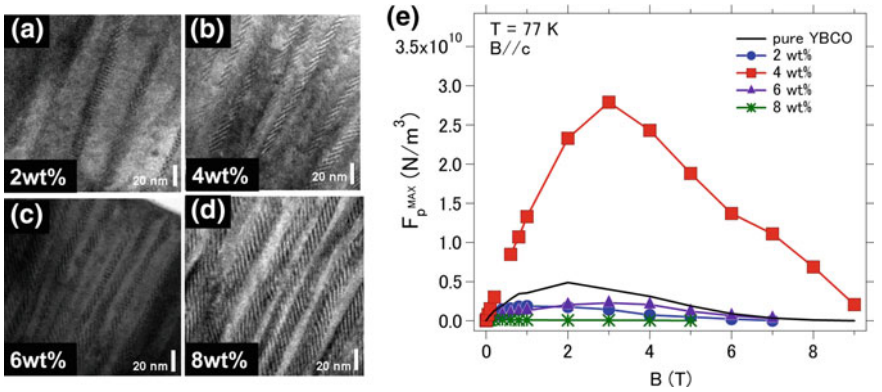

Fig. 2.15 TEM cross-sectional images of YBCO films incorporated with increasing amount of BSO: **a** 2wt%, **b** 4wt%, **c** 6wt%, and **d** 8wt%; **e** global pinning force F_p ($T = 77$ K, B//c) for YBCO films added with increasing content of BSO (2, 4, 6, 8 wt%). (Panels **a**~**d** are reproduced with permission from [117] with slight modifications)

Table 2.1 Physical parameters, calculated J_c and measured J_c (0 T, 77 K) for YBCO+BSO films

$BaSnO_3$ wt%	2	4	6	8
APCs (m^{-2}) ($\times 10^{-15}$)	0.91	2.30	5.10	6.80
d (nm)	30	21	14	12
T_c (K)	88.68	88.57	86.46	83.08
C_0 (nm)	3.8	4.28	4.3	5.5
U_0 (N) ($\times 10^{-12}$)	1.01	1.4	0.84	0.59
Calculated J_c	12	16.3	9	5
Measured J_c	0.89	1.64	0.54	0.23
J_c calc/J_c meas	13.5	9.94	16.7	22
Eff. Curr. blocking	16%	37%	50%	71%

concentration of 4 wt% BZO [3]. Analysis of the data reported by Mele et al. [117] for a series of YBCO+BSO thin films and the calculations of J_c using (2.5) are listed in Table 2.1.

From the data displayed in Table 2.1, it is obvious that the measured and the calculated values extracted from all the samples follow a similar trend with the concentration of BSO, with a maximum for 4wt% BSO-added sample. This means that increasing the amount of APCs, which lead to the reduction of the mean separation distance between the columns, does not increase J_c indefinitely. Instead, it has been shown that the enclosure of too many defects in the superconducting matrix has a detrimental effect since the resulting current-blocking effect stifles or thwarts the movement of vortices. In this regard, it can be concluded that the 4 wt% BSO content represents the best compromise between the amount of APCs and the current flow hindrance that primarily stems from the effect of current blocking. To further justify this argument, qualitative as well as quantitative analysis of the samples results from this series is given below.

It is known that the pinning force per unit length of the pinned flux line is proportional to the work done to interchange the flux line from a point to another point where the flux pinning is smaller. In this case, the equation of proportionality is written as $F_p \alpha \Delta WL/x$, where ΔW being the work done to transfer the flux line to the new point, L is the length of the flux line, and x is the extent of pinning interface. The pinning force density F_p is then customarily calculated from the temperature and/or field dependence $J_c(T, B)$ data according to the function $F_p = J_c \times B$. As shown in Fig. 2.8a, the behavior of the field-dependent $F_p(B)$ at $B//c$ direction is depicted for the 1D inclusion of BSO+YBCO samples with varying BSO concentration, as listed in the legend. Data from the undoped pristine YBCO sample and a standard (NbTi, measured at 4.2 K) sample are also shown for comparison. To elucidate additional information from this graph, Fig. 2.15e shows further split into two more figures as presented in Fig. 2.16a, b, respectively. Figure 2.16 depicts a comparative plot of the global pinning force density F_p as a function of the reduced field b for four different YBCO films engineered with four different 1D nanorod additives. As evident from the figure, the 4 wt% BSO-added YBCO film has clear superior pinning performance, both in the maximum pinning value of about 28.30 GN/m^3 and in the position of this maximum at about 0.4 reduced field. Since the effectiveness of the pinning force in all the four samples is dominated by the 1D columnar pins due to the presence of these four types of 1D ingredient, we can safely conclude that the 4 wt% BSO-added YBCO sample has a better control of the vortex pinning force associated with 1D pinning centers.

The scaling behavior of the 4 wt% BSO-YBCO sample is further fitted to the Dew–Hughes like equation $F_p = Ab^m(1\text{-}b)^n$ where A is a scaling constant and $m = 0.5$ and $n = 2.5$ are fitting parameters. The original Dew–Hughes model roughly gives $m = 1$ and $n = 2$ and the maximum F_p^{max} at $b \approx 0.25$ and 0.35 for either 1D or 3D point pinning. It should be noted here that the parameters m and n may be necessary for fitting purposes, but they might not be sufficient for the determination of the exact type of pinning associated with the samples. Important information about the dominant pinning mechanism, however, may be extracted

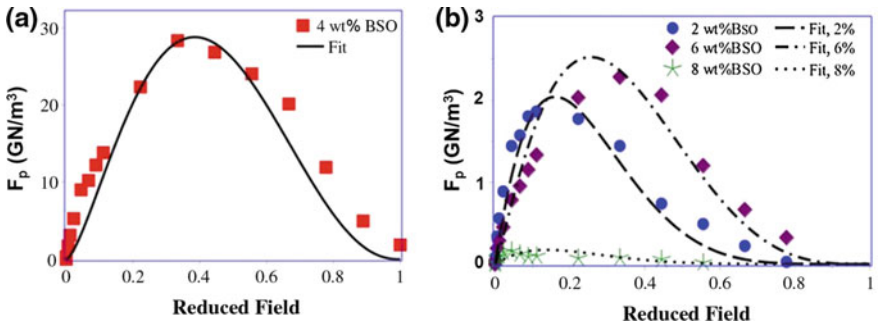

Fig. 2.16 Global pinning force F_p as a function of reduced field for **a** the 4 wt% BSO+YBCO sample and **b** the rest of the BSO-doped YBCO series of samples (2, 6, and 8 wt%). Ginzburg–Landau related fitting of the experimental data is described in the main text

from the pinning curve when vertically extrapolated down to the reduced field axis. As demonstrated in Fig. 2.16a, b, the BSO+YBCO set of samples provides different maxima reflecting the relative strength of pinning force related to their $F_p(B)$ curves and the amount of the 1D species as well. Had it been for a single pinning mechanism produced by the BSO doping with different percentage in the samples, the scaling behavior of the preceding equation should have coincided with the maximum pinning from the experimental data. But this does not seem to be the case here. Accordingly, there may at least be two different varieties of pinning force mechanisms competing for a dominant role in this set of samples. Maximum pinning for the 2 wt% BSO, the 6 wt% BSO, and the 8 wt% BSO samples corresponds to $b \approx 0.15$, $b \approx 0.31$, and $b \approx 0.035$, respectively. It can be deduced from these values that the 2, 6, and 8 wt% BSO concentration on the YBCO films acts only as uncorrelated defect point pinning with which each sample has an $I_c(B)$ value and an $F_p(B)$ value that is less compared to that of the virgin YBCO sample. This assertion is valid for the data shown in Fig. 2.16b. A reduced field $b \approx 0.4$ is, however, being verified for the 4 wt% BSO-added YBCO sample (Fig. 2.16a), a value closer to 0.7 where pinning mechanisms in a superconductor are dominated by the variation in the order parameter δl. We believe that the 4 wt% BSO contents have, to a certain degree, resulted in different reaction between its non-superconducting precipitates and the superconducting matrix. From Fig. 2.16a, b, it is conceivable to distinguish two types of pinning behaviors accompanying this sample: The highest I_c recorded for the 4 wt% BSO+YBCO sample among this series may partially be due to well-arranged nanoscale defects resulted from the concomitant crystal growth during PLD deposition of the film using a mixed target. These correlated defects later contribute to δl pinning mechanism which is responsible for the enhancement of $I_c(B)$ in the low-field regime. The second type of pinning mechanism that can be associated with the behavior of this sample is δT_c pinning which is commonly known to be the necessary precursor that enriches the value of $I_c(B)$ at high-field regime.

In the mixed state of a type II superconductor, flux pinning has a substantial effect in resisting the entry and exit of vortex flux into the material. It is apparent that the 2, 6, and 8 wt% BSO concentrations into the YBCO have created disjointed defects of sizes not in tandem with the superconducting order parameter or particularly the penetration depth, λ.

In such a situation, the unfavorable effect of the impurity sites (i.e., weak pinning centers) pushes the vortex flux lines to assume a distortive energy state. For the 4 wt% BSO sample, where pinning centers are strong, although the flux vortex lattice is little distorted, it is expected that each vortex flux line is individually pinned. It was reported that the vastly improved $I_c(B)$ and $F_p(B)$ properties in the 4 wt% BSO sample were mainly due to the effective length of the BSO defects (nanorods) which contributed to a positive superconducting energy exchange between the flux pinning mechanism and the flux density from the externally applied magnetic field [7, 117].

Figure 2.17a shows the angular dependence of the transport critical current $I_c(\theta)$ at 77 K for the 4 wt% BSO+YBCO sample. The measurements were performed

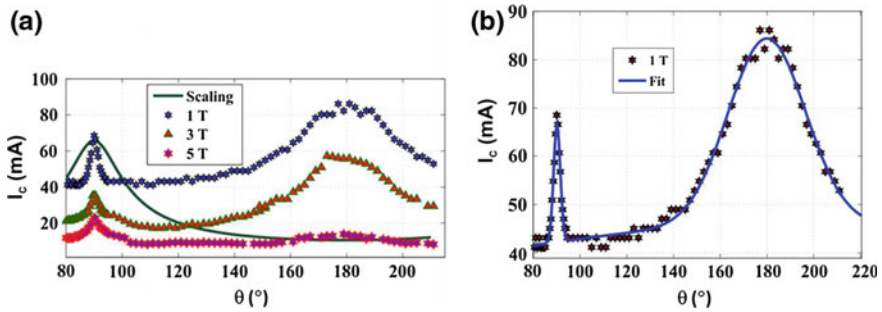

Fig. 2.17 $I_c(\theta)$ dependence for 4 wt% BSO+YBCO sample. **a** Data at 77 K and 1, 3, 5 T, with a draw of a Ginzburg–Landau scale to indicate the estimate of isotropic pinning line; **b** replot of (77 K,1 T) data fitted by a Gaussian expression

under magnetic fields of 1, 3, and 5 T, respectively. The field orientation angle θ points to the direction of the applied magnetic field with respect to the *c*-axis of the film.

With the aim to better understand the cause of the flux pinning mechanisms which is the main cause of driving the vortex pinning force density of a high T_c superconductor in a magnetic field, it is of crucial importance to discuss the angular dependence $I_c(\theta)$ data taking into consideration the response of the sample to a varying field values across a wide range of the measuring angles. We shall start the discussion from the viewpoint of the Blatter model [33, 34]. In a YBCO superconductor although generally regarded as less anisotropic, the $I_c(\theta)$ can be found to have strong dependence on the orientation of the applied magnetic field with respect to the crystallographic axis directions. Indeed, this was the case when the APCs are accommodated in the pristine YBCO films so as to improve the pinning potential in the material. As viewed from Fig. 2.17a, the anisotropy of the crystallographic axes *a* and *b* with their level located along the cuprate plane can show sharp but relatively small peak at $\theta = 90°$ when the applied field *B is parallel to ab* plane (*B//ab*). The physical meaning of the isotropic or intrinsic pinning of this orientation is that the vortices revolving parallel to the *ab* plane are strongly pinned by the presence of point defects such as 1D- and 3D-APCs, and the weakly superconducting layers between the CuO_2 planes. The physical properties of the isotropic contribution to the overall pinning landscape is therefore largely explained by the Blatter scaling approach for the vortex flux line in the anisotropic Ginzburg–Landau (GL) theory. The Blatter model has shown that the anisotropy of a superconductor can have an anisotropic parameter, ε:

$\varepsilon = \frac{1}{\gamma} = \frac{\lambda_{ab}}{\lambda_c} = \frac{\xi_c}{\xi_{ab}} = \sqrt{\frac{m_{ab}}{m_c}}$ where m_{ab}, m_c and λ_{ab}, λ_c, ξ_{ab}, ξ_c are the mass tensor and the anisotropic superconducting parameters in the *a*, *b,* and *c* crystallographic directions. The effective magnetic field in play in this case is given by $B(\theta) = \varepsilon_0 B$. The Blatter scaling model can then be given for anisotropic

superconductor as $\varepsilon_\theta = \sqrt{sin^2\theta + \varepsilon^2 cos^2\theta}$ with θ being the angle between the applied field B and the ab crystal plane.

The scaling method used to produce Fig. 2.17a can hardly scale the seemingly isotropic contribution of the 4 wt% BSO-doped YBCO sample. The reasons for the discrepancy between the experimental data and the scaled fit can be viewed from the points that the scaling approach assumes the material to be strictly isotropic so that the scaling coefficient $\gamma \approx 5$–7. The reason mentioned in the preceding line could lead to the assertion that the pinning behavior of the 1D BSO species of existing concentration in YBCO film is also not isotropic enough apart from the narrow window in the vicinity of $85° \leq \theta \leq 105°$ where pinning mechanism is due to random defects or uncorrelated disorder. However, the scaling approach has no answer to the huge and rather extended peak centered around $\theta = 180°$. Moreover, the angular-dependent $J_c(\theta)$ for YBCO films deposited on different substrates shows that it is extremely difficult to account for the combined effect of random defects and mass anisotropy when the $J_c(\theta)$ data are mapped across a wide angular range. It was concluded that the effect of correlated pinning structure in the samples with the maximum at both $\theta = 90°$ and $\theta = 180°$ cannot be accounted for by the anisotropic scaling [102].

Since the data presented in Fig. 2.17a are highly anisotropic across the advancing angular range, we use a Gaussian statistical expression to account for the enormous pinning effect of the 4 wt% BSO nanocolumns in the vortex flux pinning mechanism of this YBCO sample. Figure 2.17b shows the model fit to the 1 T $I_c(\theta)$ data.

The Gaussian statistical expression used to fit the data shown in Fig. 2.1 can be written as

$$I_c(\theta) = I_{(c(0))n} \exp \sum_{n=1}^{3} \left(- \left(\frac{\theta - \beta_n}{\delta_n} \right) \right)^2 \tag{2.7}$$

where the numerical coefficients for the quantities appearing in the (2.6) are shown in Table 2.2.

In the fit shown in Fig. 2.17b, the θ values across the angular range are normalized by means of 131.4° where the coefficients are 95% confidence bound and the goodness of fit was $R^2 = 0.99$. From the data shown in Table 2.2, it is clear that the data of the sample are divided into three regions, the isotropic peak, the plateau, and the enormously huge anisotropic peak at the far right of the curve. Unlike the original anisotropic GL model where the isotropic peak shows elliptical symmetry and a concave pinning plateau elsewhere, the statistical estimation using (2.7) has at

Table 2.2 The angular quantities used in fitting the $I_c(\theta)$ for the 1 T field shown in Fig. 2.16

Parameter	n = 1	n = 2	n = 3
$I(0)_n$	38.4	24.33	46.03
β_n	1.16	−0.99	1.49
δ_n	0.56	0.05	8.40

least roughly accounted for the effect of the 1D pinning on the vortex configuration feature of the sample measured at 1 T.

Indeed, the addition of 4 wt% BSO into YBCO sample has contributed to better isotropic feature at a narrow angular range, as characterized by a sharp peak centered at $\theta = 90°$. The anisotropy of $I_c(\theta)$ in the intermediate region is rather short lived but shows a horizontal feature just before the *c*-axis anisotropy dominates.

$BaHfO_3$ (BHO) Nanocolumns

Recently, $BaHfO_3$ (BHO) nanorods became trendy since BHO has been found to give strong pinning without significant depression of the T_c of the superconducting matrix. Tobita et al. [119] first reported that a BHO-doped $GdBa_2Cu_3O_y$ (GdBCO) film is deposited by PLD on IBAD-MgO substrate. The most interesting feature of BHO nanocolumn addition was reported as J_c is undepressed by increasing thickness of the film (Fig. 2.18).

The SmBCO/BHO system was extensively studied in Nagoya University by Y. Yoshida group [5, 8, 124–126]. Low-temperature growth (LTG) SmBCO/BHO films show striking performance with $F_p^{max} = 28$ GN/m^3 and $B_{irr} = 15$ T [8] as a result of the unique linearity and the narrow angle distribution of the BHO nanorods.

Very recently, it was found that BHO-added SmBCO films prepared by LTG method present large values of F_p below 77 K. As shown in Fig. 2.19, maximum flux pinning forces (F_p) of 105 GN/m^3 in 9.0 T at 65 K and 405 GN/m^3 in 9.0 T at 40 K have been obtained thanks to the high density and small size of the nanorods embedded in the superconducting matrix [5]. Furthermore, the increase in self-field J_c of GdBCO-BHO films deposited on single crystals with artificial grain

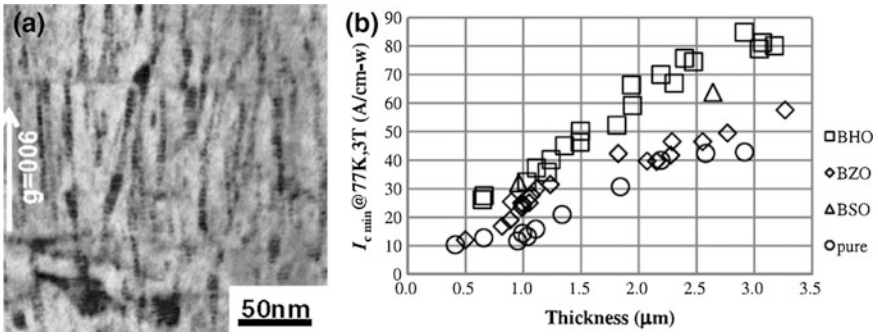

Fig. 2.18 **a** Cross-sectional TEM images of GdBCO-coated conductors incorporating BHO nanorods. **b** Thickness dependence of I_c at 77 K and 3 T for BHO-doped GdBCO CCs compared with BSO- and BZO-doped GdBCO CCs and pure GdBCO CCs. (Figures reproduced with permission from [123])

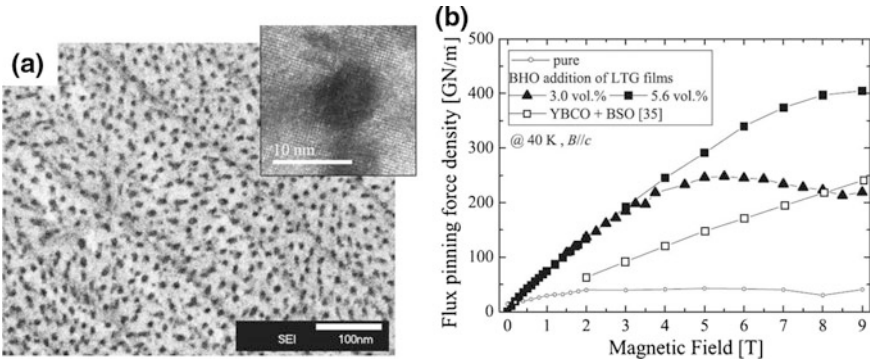

Fig. 2.19 **a** Plan-view TEM images of SmBCO films with 4.1 vol.% BHO content, fabricated with alternating target technique by pulsing the BHO target 3 times per cycle. **b** Magnetic field dependence of flux pinning force density F_p at 40 K for 0 (pure), 3.0, and 5.6 vol.% BHO-doped $SmBa_2Cu_3O_y$ LTG films, and a $BaSnO_3$-doped $YBa_2Cu_3O_y$ film reported by Mele et al. [3]. (Figures reproduced with permission from [9] with slight modifications)

boundaries by flux pinning of the Abrikosov–Josephson vortices by BHO nanorods [126] was demonstrated. All the results described previously were obtained on single crystals. The deposition of GdBCO+BHO has been tried on metallic substrates as well [9], obtaining very large $F_p^{max} = 23.5$ GN/m^3 and outstanding value of irreversibility field $B_{irr} = 15.8$ T.

Other Oxide Nanocolumns

Other than perovskite BMO (M = Zr, Sn, Hf) nanorods, Harrington et al. [127] reported excellent pinning performance at 77 K via the incorporation of very stable RE_3TaO_7 (RE = Er, Gd, Yb) pyrochlore nanorods in YBCO PLD films without significant depression of T_c. The presence of additional nanoparticles (Fig. 2.20a) yields increase of the J_c in the whole range of angles, while the effect of the nanorods becomes predominant at high fields (Fig. 2.20b, c).

Feldmann et al. [128] successfully added a high density of double perovskite Ba_2YNbO_6 nanorods into PLD thin films, and substantially, enhanced pinning was achieved in their sample: maximum global pinning forces of 32.3 GN/m^3 (75.5 K) and 122 GN/m^3 (65 K).

2.3.3 Two-Dimensional APCs (2D-APCs)

Two subcategories of 2D-APCs can be mentioned: (i) nanolayers and (ii) grain boundaries

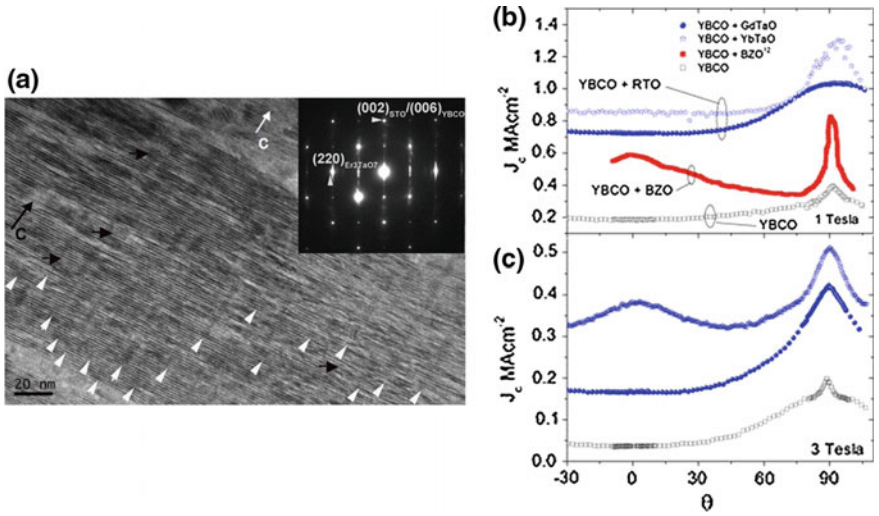

Fig. 2.20 *Left* **a** Microstructure of a typical YBCO+RTO film. TEM cross-sectional image of YBCO+5 mol% ErTaO film grown at 765 °C and 10 Hz, inset, proves the structure of the rare earth tantalate phase is the pyrochlore Er_3TaO_7. Vertical arrows show positions of the self-assembled nanorods, and horizontal arrows show the positions of some of the random nanoparticles. *Right* Angular dependence of the critical current density at 77 K for standard YBCO, YBCO+BZO (~7 mol%) and YBCO+RTO films: **b** 1 T and **c** 3 T. (Figures reproduced with permission from [127] with slight modifications)

2.3.3.1 Nanolayers as 2D-APCs

As understood in the early 1990s [135, 136], the critical current of thin films does not increase indefinitely by increasing thickness. The reason [137–142] is that the quality of thin film, and hence J_c, is best near the substrate, and as the film is grown thicker, current-blocking defects (misoriented crystallites, cracks or voids) become more prevalent, depressing the critical current.

In their remarkable works, Foltyn et al. [38, 143] proposed a revolutionary way to have thick YBCO films increased critical current: Six YBCO-CeO_2 layers were deposited on buffered metal substrates by PLD, resulting in a 3-μm-thick film where critical current exceeded 1000 A/cm^2. It was thus demonstrated [38, 143] that by periodically inserting 30-nm CeO_2 layers every 0.5 μm or so in a thick YBCO film (Fig. 2.21a), a high critical current density is maintained. As shown in Fig. 2.21b, single-layer coatings do not reach 600 A/cm width unless the thickness is more than 4 μm. However, six 0.55-mm-thick YBCO layers, separated by 40-nm-thick CeO_2 layers, have a J_c of 4 MA/cm^2—nearly that of a single 0.55-mm layer. The key is in the multilayers' ability to preserve thin-film J_c values, as indicated by the arrow (Fig. 2.21). This amazing result marked a significant advance in coated conductor technology.

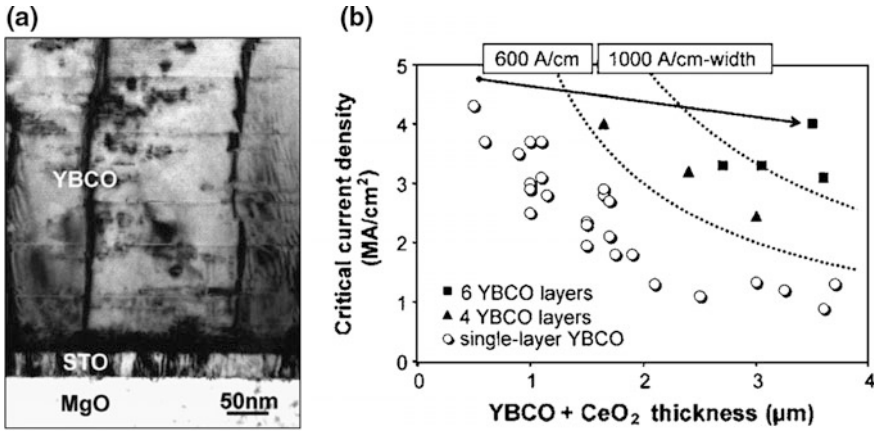

Fig. 2.21 **a** Transmission electron microscope image of a pulsed laser deposition YBCO+CeO_2 multilayer on a single-crystal MgO substrate with a $SrTiO_3$ buffer (**b**). Comparison of single-layer and YBCO/CeO_2 multilayer films. (Reproduced with permission from [143])

After this breakout, research on multilayers flourished and a variety of multilayered and quasi-multilayered structures have been tried: Y_2O_3/YBCO [144, 145], YBCO/DyBCO [146, 147], YBCO/EuBCO [148], YBCO/NdBCO [149], Y_2BaCuO_5 (Y-211)/YBCO [150], YBCO/YSZ [151], $SrRuO_3$/YBCO [152], YBCO+$BaZrO_3$/CeO_2 [153], YBCO/$BaZrO_3$ [154], YBCO/$SrTiO_3$ [155], YBCO/$LaCaMnO_3$ [156] YBCO/ZnO [157], $Sm_{1.04}Ba_{1.96}Cu_3O_y$/$Sm_{1.08}Ba_{1.92}Cu_3O_y$ [158], and so on. The general common effect of multilayer approach is an enhancement of J_c in magnetic field, sometimes combined with weak *c*-axis-correlated pinning.

All these structures involve *c*-axis-oriented YBCO layers stacked with different kind of oxides. Horii et al. [159] proposed a multilayered structure alternating *a*-axis-oriented YBCO [160] and semiconducting PrBCO interlayers. The PrBCO layers act as 2D-APCs. The consequence is a weakening of the intrinsic pinning along the *ab* plane and enhancement of the *c*-axis-correlated pinning [161, 162].

2.3.3.2 Grain Boundaries as 2D-APCs

The grain boundaries in the HTS show the Josephson-like behavior when the misorientation angle of adjacent grains becomes ten degrees or more. This causes a weak coupling due to which J_c rapidly decreases at the grain boundaries. However, the small-angle grain boundary can be considered as a dislocation array, and there is a possibility to act as strong pinning center when the misorientation angle is small. This is one of the natural pinning previously mentioned. Matsumoto et al. [163] have reported the use of grain boundaries as effective pinning centers in GdBCO films. By varying the oxygen partial pressure during deposition, the size of the

grains continuously changed from 196 to 92 nm. J_c and F_p^{max} increase with the reduction of the grain size, suggesting that the (001) tilt grain boundaries act as pinning centers in the film and that the improvement of F_p appears because the density of pinning centers increases as the grains become smaller. The maximum F_p for the sample of which grain size is 92 nm is about 15 GN/m^3 at 77 K, *B*//*c*, approaching the value of NbTi at 4.2 K.

Another type of grain boundary, in this case as 2D artificial pinning center, comes from the catalytic effect of silver during the growth of YBCO as was demonstrated in A. Crisan's group [164, 165]. It was shown that Ag nanodots (in substrate decoration and/or quasi-multilayer approach) have a twofold beneficial effect: (i) allow the growth of much thicker (up to 5 μm) YBCO films without a very strong decrease in the critical current density (thus increasing the critical current) and (ii) promoting a columnar growth of YBCO. The surface of the cylinders, which in the case of BZO-doping is also entangled with BZO nanorods, provides very strong pinning centers. Their 2D character was demonstrated by a Dew–Hughes-Like analysis of the reduced field dependence of the global pinning force [166].

2.3.4 *Three-Dimensional APCs (3D-APCs)*

For practical applications of YBCO superconductors, there is a very desirable feature which is the isotropic character of J_c with high values under a wide range of applied magnetic field under various orientations. Therefore, considerable efforts have been made to prepare superconducting thin films incorporating 3D-APCs.

Pioneering work on 3D-APCs addition was published in 2004 by Haugan et al. [10] with incorporation of disk-shaped Y211 nanoparticles in YBCO film by PLD (Fig. 2.22a). The Y211 addition clearly shows improvement of J_c in magnetic fields due to enhanced pinning (Fig. 2.22b).

Extensive work on the introduction of 3D-APCs in YBCO films has been made by several groups using TFA-MOD method. It was reported that the highly densified nanoparticles can be introduced into the YBCO films by mixing foreign elements of proper quantities with the starting solution including Y, Ba, and Cu. In the BZO case, nearly isotropic angular dependence of J_c is reached [167] with F_p^{max} of 22 GN/m^3 (77 K, *B*//*c*) [168]. At its time, this result from X. Obradors group (ICMAB Barcelona) was the best pinning performance reached with isotropic APCs (Fig. 2.23a, b). Other effective isotropic pinning centers added to YBCO by MOD process are Y_2O_3, $BaCeO_3$, and Ba_2YTaO_6 [169]. It is worth noting here that the round-shaped particles dispersed in the superconducting film by MOD are randomly oriented because there is no preferred crystallographic orientation between the superconducting matrix and the foreign phase.

PLD process was also extensively used to incorporate 3D-APCs in superconducting thin films. First of all, a Sm-rich SmBCO target, with composition $Sm_{1+x}Ba_{2-x}BaCuO_y$, was used for ablation in the PLD process [170–174]. Low T_c 3D

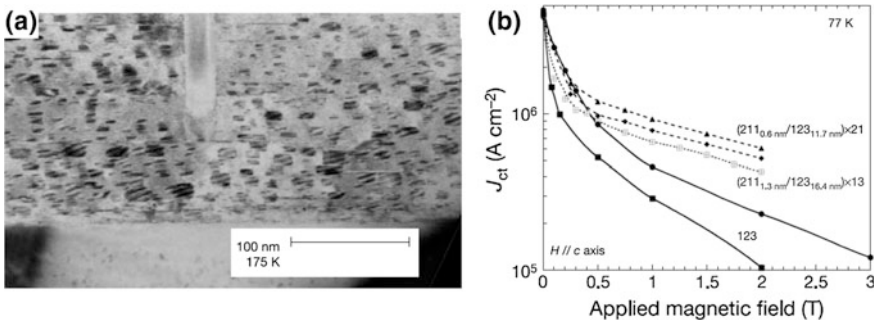

Fig. 2.22 **a** Transmission electron micrographs of YBCO+Y211 films, showing repeated layering structure and nanoparticle formations; **b** critical current density as a function of applied magnetic field for YBCO+Y211 films compared to pure YBCO films (*solid lines*) prepared by PLD (*filled squares*) and MOD (*filled circles*). Multilayer films (*dashed lines*) were measured for different Y211 and YBCO parameters, and for samples from the same deposition run (*triangles and diamonds*). (Reproduced with permission from [10])

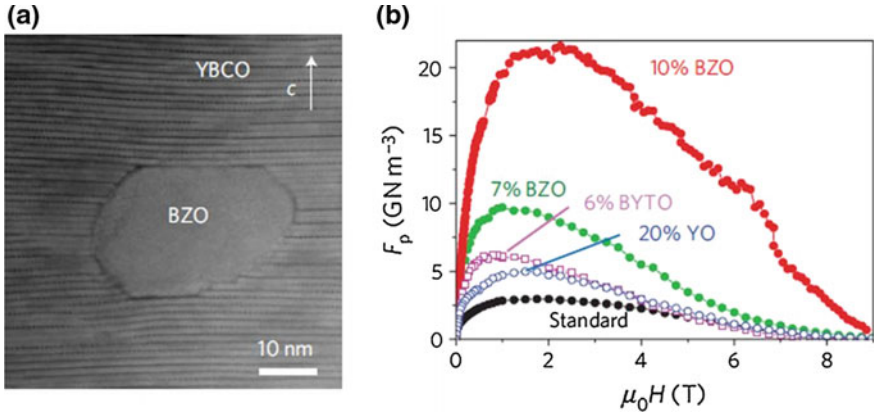

Fig. 2.23 **a** High-magnification cross-sectional TEM micrograph of a BZO nanoparticle embedded in YBCO thin film grown on STO; **b** pinning force versus magnetic field at 77 K in a series of YBCO MOD films added with several kinds of nanoparticles. (Both panels reproduced with permission from [168])

nanoparticles are randomly dispersed in the superconducting matrix due to the local compositional fluctuation, and significant improvement in the pinning properties has been achieved. Very high values $J_c = 0.37$ MA/cm^2 (77 K, 5 T, *B*//*c*) and $F_p^{max} = 23$ GN/m^3 (77 K, *B*//*c*) were reported for the first time in 2006. Additionally, B_{irr} of the SmBCO films reached very high values, up to 12 T (77 K, *B*//*c*).

Alternatively, the introduction of nanoparticles into YBCO film was made by switching the superconducting target and the dopant target in an alternating manner. Under selected experimental conditions, instead of multilayered structure with

separation between the two phases, nanoparticle structure embedded into the film was obtained. The 3D-APCs incorporated were Y211 [175–177], Y_2O_3 [178–182], perovskites ($BaIrO_3$ [183], and $BaHfO_3$ [184]). Metallic elements such as Ag, Au [185, 186], and $Gd_2Ba_4CuWO_y$ compound [187] were consequently employed.

A third method that allows the creation of 3D-APCs into the superconducting films was developed by using the target surface modification method [188, 189]. In this method, a small piece of the sintered APC material such as Y_2O_3 is placed onto the YBCO target and together, and they are used for the usual PLD deposition process. This technique has the merit to introduce the nanostructure into epitaxial thin films through a very simple procedure.

Y_2O_3 nanoparticles are incorporated in YBCO matrix and show epitaxial relationship with YBCO: (001)YBCO//(001)Y_2O_3, and [100]YBCO//[110]Y_2O_3 crystallographic orientation. That is, the *a*-axis of the Y_2O_3 nanoparticles is oriented 45° with respect to the YBCO *a*-axis, while the same out-of-plane (*c*-axis) orientation is apparently preserved in the hybrid structure. In YBCO films where 3D-APCs are incorporated, additional defects such as stacking faults are also present, most probably playing the role of additional pinning centers [178, 189] (see Fig. 2.24a). The Y_2O_3 particles are homogenously dispersed into YBCO matrix, and consistently, the J_c angular dependence does not show any peak at *B*//*c* orientation (Fig. 2.24b).

More recently, Xu et al. [11] proposed a heat treatment-based method via direct ablation of pure YBCO target at high temperature of 830°C instead of the usual 800 °C used by other workers. Without any addition of secondary phase onto the target or surface modification, dispersed Y_2O_3 particles are obtained due to different kinetic energy during the growth.

Mele et al. studied systematically the effect of increasing additions of Y_2O_3 in YBCO thin films [189]. Similar to BSO compound, the Y_2O_3 oxide addition increases the amount of APCs according to the size of the area of the sliced piece

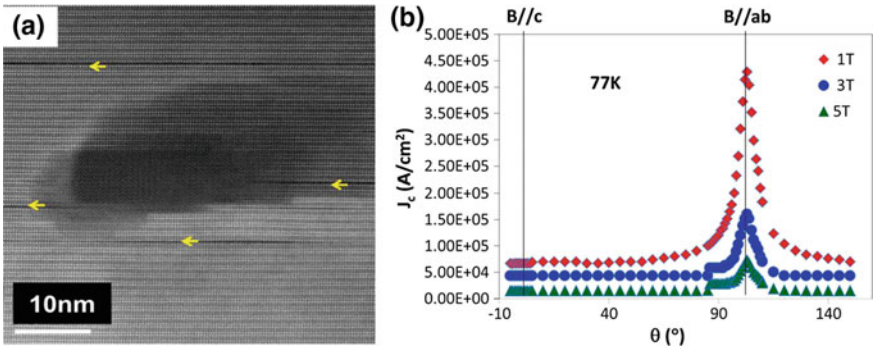

Fig. 2.24 **a** High-resolution transmission electron microscopy (HRTEM) image of a Y_2O_3 nanoparticle embedded in a superconducting matrix. *Arrows* indicate $Y_2Ba_4Cu_8O_{16}$ (Y248) intergrowths (i.e., stacking faults); **b** angular dependence of critical current density (77 K, $B = 1$, 3, 5 T) for YBCO+Y_2O_3 2.51 A%. (Both figures reproduced with permission from [189])

placed onto the superconducting target, but the resulting critical currents and pinning force density were not always proportional to Y_2O_3 contents, as deduced from the study of the whole series of the samples [189]. For example, the 9.22A% Y_2O_3 film presents a global pinning values lower than the standard YBCO film, while the 5.44 A% Y_2O_3 sample produced a global pinning force of 14.3 GN/m^3 at 77 K, twofolds the value obtained in the 2.51A% Y_2O_3 sample which is comparatively similar to the global pinning of NbTi tape at 4.2 K [190]. This value is also very close to the value obtained for the YBCO films with $BaZrO_3$ nanorods, but with a much less depression in the superconducting critical temperature.

Nanoparticle defects such as Y211 and Y_2O_3 are experimentally proven to increase the strength of pinning centers so that vortices surrounding them can bend to create discrete trapped segments [191–193]. In this context, it is foreseeable to estimate the maximum critical current J_c from the depinning of curve segments which are fixed by two consecutive nanoparticles separated by a distance *d*. The analytical expression resulting from the above argument can be written as

$$J_{c,\max} = \frac{\Phi_0}{4\pi\mu_0\lambda_{ab}\lambda_c d}\ln\frac{d}{\xi_c} \tag{2.8}$$

where Φ_0 is the flux quanta, μ_0 is the magnetic permeability, λ_{ab} and λ_c are the London penetration depths in the *ab* plane and along the *c*-axis, respectively, and ξ_c is the coherence length along the *c*-axis. Analysis of the data reported by Mele et al. [189] for a series of YBCO+Y_2O_3 thin films and the calculations of U_0, J_c by using (2.8) are listed in Table 2.3.

Parameters extracted for YBCO at 77 K are $\lambda_{ab} = 0.35$ μm, $\lambda_c = 2.4$ μm, $\xi_c = 0.6$ nm, and the mean separation between Y_2O_3 particles $d \sim 18$ nm, as approximated from TEM images [189] for Y_2O_3 5.44A% sample, and the estimated J_c (77 K, self-field) is 6.40 MA/cm^2. The relative consistency with the experimental value of 3.21 MA/cm^2 demonstrates that Y_2O_3 particles act as good pinning centers. Indeed, the effective current blocking is only 13% of J_c and therefore no much of a hindrance for the supercurrent to percolate avoiding the pinning barriers (normal cores). For the 9.22A% sample, the mean separation distance between

Table 2.3 Physical parameters, calculated J_c, and measured J_c (0 T, 77 K) for YBCO+Y_2O_3 films

Y_2O_3 content	2.51A%	5.44A%	9.22A%
Amount of APCs (m^{-2})	1.75×10^{15}	2.68×10^{15}	5.23×10^{15}
T_c (K)	89.26	89.2	87.78
d (nm) [36]	20	18	12
Calculated J_c	5.93	6.4	7.4
Measured J_c	2.62	3.21	0.89
J_c calc./J_c meas.	2.26	1.99	8.31
Effective current blocking	10%	13%	32%

particles is estimated to be $d \sim 12$ nm. Hence, current calculation has given J_c (77 K, self-field) = 7.40 MA/cm^2, while the experimental value is merely 0.89 MA/cm^2. The depression of J_c in the 9.22A% sample may be due to the presence of a larger density of non-superconducting particles such as Y248 intergrowth compound which contribute to about 32% current blocking. Interestingly enough, the presence of Y248 intergrowths can play two opposite roles in the superconductivity of the sample. While large sizes of the Y248 intergrowths can result in a poor superconducting material, they may also act as good pinning centers provided that their sizes are comparable to the coherence length. However, in the case of this particular sample, Y248 is present in the form of disks situated perpendicular to c-axis of the film with lengths of several hundreds of nanometers which in turn impede the motion of vortices.

It is worth noting that the pinning performance of the nanorods at 77 K is superior with respect to the Y_2O_3 nanoparticle doping. However, in the case of eventual decrease in T_c due to the spherical inclusion of foreign species, the pinning performance of nanorods considerably deteriorates. This behavior was first observed by Mele et al. [188] as it was later confirmed in recent years in the work of Xu et al. [11]. They reported detailed analysis of YBCO+Y_2O_3 films in a wide range of operating temperatures. Their findings showed that at 4.2 K and 16 T, the Y_2O_3-YBCO film attains $F_p = 1000$ GN/m^3, about 30% higher than the 7.5% Zr-added REBCO prepared by MOCVD [11] where BZO nanorods are integrated into the film.

There are different techniques used for the approximation of the very high values of J_c in superconductors with nanoscale pinning centers. Since the electric field vector within a conductor satisfies a vector wave $\nabla^2\widehat{\mathrm{B}} + \kappa^2\widehat{\mathrm{B}} = 0$, we consider a vortex flux line as a tiny cylinder of radius a lying along the z-axis where J_c has only a z -axis component. The waveform due to the field generated by the interaction of the vortex flux line pinned by a nanoparticle in the presence of the externally applied field can be expressed in terms of the Bessel's equation of order zero such that

$$\frac{d^2\widehat{B}_z(\rho)}{d\rho^2} + \frac{1}{\rho}\frac{d\widehat{B}_z(\rho)}{d\rho} + \kappa^2\widehat{B}_z(\rho) = 0 \tag{2.9}$$

where $\rho(z)$ is a local coordinate for the vortex flux line, and κ is a wave number. The solution to the above equation yields the field generated by the vortex interaction with a potential pinning site and can be given by

$$\widehat{B}_{z,\mathrm{v}}(\rho) = \widehat{B}_{(0),\mathrm{v}}\frac{I_0(\kappa\rho)}{I_0(\kappa a)} \tag{2.10}$$

where $\widehat{\mathrm{B}}_{(0),\mathrm{v}}$ is the field at the surface of the film. The I_0 is the zero-order Bessel's function of the first kind. Hence, the J_c within the vortex flux line is the consequence of the film's conductivity and the interactive field generated.

$$\widehat{\mathrm{J}}_{z,\mathrm{v}}(\rho) = \sigma \widehat{\mathrm{B}}_{(0),\mathrm{v}} \frac{I_0(\kappa\rho)}{I_0(\kappa a)} \tag{2.11}$$

Therefore, at near zero field, $\widehat{\mathrm{B}}_{(0)}$, and $\widehat{\mathrm{J}}_{c,\mathrm{v}}$ distributions are nearly uniform. Note that the term σ can "mathematically" be dropped from (2.10) since $\sigma \rightarrow \infty$ for a superconductor. In this case, (2.10) reduces to the form shown in (2.9) and the field vector essentially extends the current vector over a finite length of the vortex flux line. The asymptotic behavior of the high J_c across the field is therefore estimated using the large argument of the Bessel's function of the first kind.

$$I_n(x) = \sum_{\kappa=0}^{\infty} \frac{(-1)^{\kappa}}{\kappa!\Gamma(\kappa+p+1)} \left(\frac{x}{2}\right)^{2\kappa+p} \tag{2.12}$$

where I_n is the Bessel's function of integer order $n = 0, 1, 2, \ldots$, x is any positive quantity, $p = 0.5$, $\kappa = 0, 1, 2, \ldots$, and $\Gamma(\kappa+p+1) = \frac{(2\kappa+1)}{2^{2\kappa+1}\kappa!}\sqrt{\pi}$. The asymptotic behavior of (2.11) yields the analytical expression shown below in (2.12).

$$I_n(x) = \sqrt{\frac{2}{\pi x}} \cos\left[\pi x - \left(\frac{n\pi}{2}\right) - \frac{\pi}{4}\right]; \quad \text{thus,} \quad J_c(B) = \sqrt{\frac{2}{\pi x}} \cos\phi \tag{2.13}$$

where $\phi = \left[x - \left(n\frac{\pi}{2}\right) - \frac{\pi}{4}\right] \approx 0.007°$ is the angle at which the pinned vortex can bend.

The maximum attainable J_c is 40 MA/cm^2. This value corresponds to the maximum current density through the normal direction or the z-axis of a vortex core spinning around the vicinity of magnetic field $B = 0$ T [193]. Figure 2.25a shows

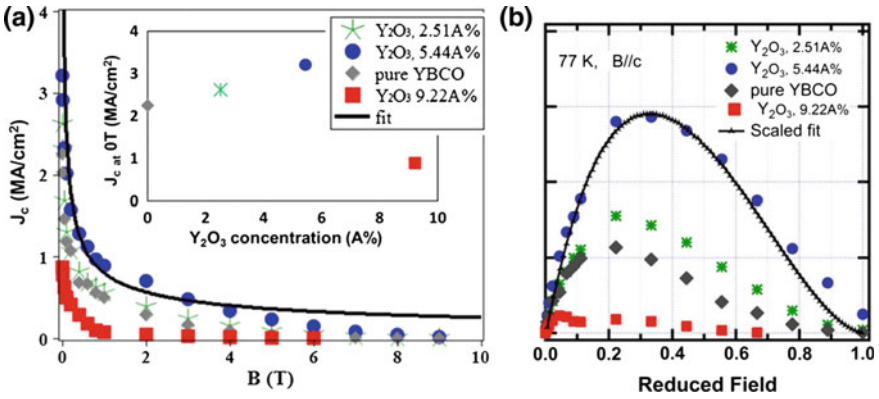

Fig. 2.25 **a** Critical current density, J_c, versus magnetic field, B (77 K, $B//c$), for a pure YBCO film and doped YBCO films with Y_2O_3 nanoparticles. Fit based on single vortex dynamics is plotted along with experimental data. Inset shows the behavior of $J_c(B = 0)$ in a function of Y_2O_3 concentration. **b** Global pinning force, F_p, versus the reduced field $b = B/B_{irr}$ at 77 K and $B//c$. Theoretical, $b = 0.35$ is within 2% of the experimental error. Note that $F_p = 1.3$ GN/m^3 at $b = 1$. (Reproduced with permission from [189])

the field dependence $J_c(B)$ for the standard YBCO together with YBCO samples added with 2.51A%, 5.44A%, and 9.22A% Y_2O_3. A fit based on (2.11) and (2.12) is also depicted in the figure. In comparison with the standard YBCO film, the 5.44A %, Y_2O_3 sample shows a good field-dependent J_c up to 4 T. Beyond 4 T however, the J_c of all samples decreases below the curve of the depinning current density. As the low-field regime is known to characterize the single vortex dynamics, the $J_c(B)$ of the 5.44A%, Y_2O_3 sample is seen to have a quite good consistency with the positive effect of Y_2O_3 nanoparticles.

For YBCO samples added with 2.51A%, 5.44A%, and 9.22A% $Y_2O_{3,,}$ the minimum pinned vortex core length is estimated to be about 6.5%, 8.0%, and 2.2%, respectively [189].

2.3.5 Segmented 1D-APCs

For practical applications, the merits and drawbacks of continuous nanorods (1D-APCs, high J_c but anisotropic pinning) and randomly distributed nanoparticles (3D-APCs, isotropic pinning but lower J_c) suggested investigating the intermediate anisotropy range of vortex pinning between the two limits.

This kind of approach has been studied at first by Horide et al. [194]. By means of PLD, they prepared multilayered samples comprised of pure YBCO layers alternating with YBCO layers containing nanorods. In this way, segmented BZO nanorods are produced because the nanorods nucleate and grow exactly above the upper portion of nanorods underneath the pure YBCO layer. The thickness of the layers containing nanorods can be easily varied by changing the number of pulses in PLD ablation, so that from "short nanocolumns" (still 1D-APCs) it is possible to gradually pass to "nanoparticles" (3D-APCs, but regularly distributed).

As a result, the *c*-axis-correlated peak in the angular current plot becomes gradually small. Also, the critical exponents at the vortex liquid–solid transition change from the Bose glass to the vortex glass.

The effect of segmented BSO nanorods on B_{irr}, T_c, J_c characteristics has been systematically investigated, and flux pinning mechanisms have been discussed in recent work of Matsumoto et al. [195, 196]. The thicknesses of superconducting layers of YBCO (l_s) and pinning layers of YBCO+BSO (l_p) have been controlled, and several samples have been prepared combining $l_p = 90$, 60, 30 nm and $l_s = 45$, 30, 15 nm (Fig. 2.26a).

By applying a "harmonic oscillator" approach based on the Bose glass state, the J_c of samples can be calculated as

$$J_c^{segmentedB//c} = \frac{\Phi_0}{16\pi\mu_0\lambda_{ab}^2\xi_{ab}}\left[\frac{l_p}{l_p + l_s}\right] \tag{2.14}$$

In the *B*//*c* case.

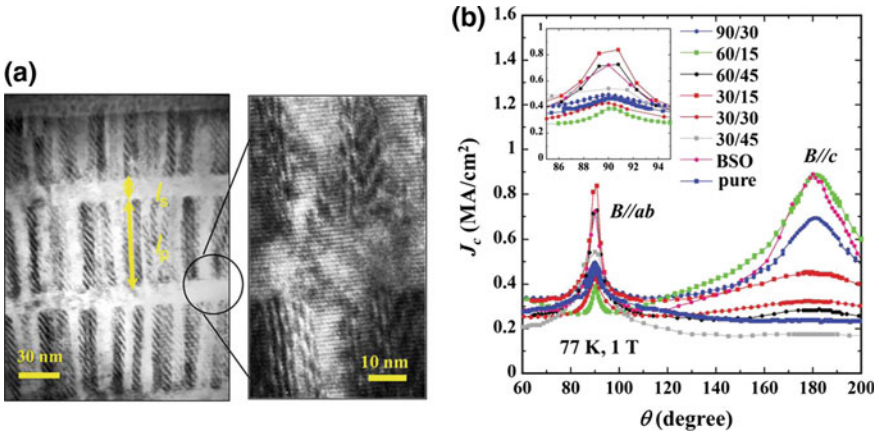

Fig. 2.26 **a** TEM cross section of PLD-YBCO film with length controlled nanorod segments (60/15 configuration). **b** Field angular dependences of $J_c(\theta)$ at 77 K, 1 T for YBCO-BSO film, YBCO-BSO/YBCO multilayered films with 90/30, 60/15, 64/45, 30/15, 30/30, 30/45 configurations. Inset shows a magnification of *B//ab* peak. (Both figures reproduced with permission from [195])

This expression must be modified in the *B//ab* case:

$$J_c^{segmentedB//ab} = \frac{B_c^2 \pi \xi_{ab} a_0^2}{2\mu_0 \Phi_0 d^2} \left[\frac{2C_0}{l_p + l_s}\right] \tag{2.15}$$

where a_0 is the vortex line spacing, $a_0 = (\Phi_0/B)^{1/2}$, C_0 is the radius of columns, and d is the mean distance between them.

The tendencies of J_c ($B//c$) > J_c ($B//ab$) were observed for the films with large l_p, but the opposite ones of J_c ($B//c$) < J_c ($B//ab$) for the films with small l_p (Fig. 2.19b). This behavior suggests that a vortex of length l_p+l_s is strongly pinned over a portion of length l_p and the pinning effect is degraded at $B//c$ when l_p becomes small, however, recovered at $B//ab$ by additional pins involved in the films.

Significant variation was considered by Horide et al. [197]: Instead of superconducting YBCO layers, semiconducting perovskite PrBCO layers are alternated with YBCO+BSO layers. Main result is that the *c*-axis-correlated pinning was weakened by the PrBCO layers in the multilayers.

2.3.6 *Combined One-Dimensional and Three-Dimensional (1D+3D) APCs*

Another nanoengineering approach to control the angular dependence of J_c in the intermediate range is the combination of APCs of different dimensionality.

Two ways are possible to obtain combined one-dimensional and three-dimensional (1D+3D) APCs in YBCO films: (i) simultaneous combination of columnar defects (1D) and nanoparticles (3D) in hybrid films by ablation of a single target and (ii) separating columnar defects and nanoparticles in multilayers by alternate ablation of two targets.

2.3.6.1 Hybrid YBCO Films with Mixed 1D+3D-APCs

One of the earliest reports on hybrid films with 1D+3D-APCs incorporation was made by Mele et al. [198] using a YBCO+4wt% BZO-mixed target whose surface was modified by sticking a 2.5A% Y_2O_3 sector on it. They formed YBCO films incorporating 1D-APCs (BZO nanorods) and 3D-APCs (Y_2O_3 islands) at the same time. In the double-doped sample, the angular dependence of J_c showed an intermediate behavior, with broad peak at *B//c* due to the flux pinning by *c*-axis-correlated defects, combined with a plateau, due to the flux pinning by isotropic pinning centers. Both BZO nanorods parallel to the *c*-axis and Y_2O_3 nanoparticles randomly dispersed inside the YBCO matrix were consistently observed in the cross-sectional TEM images. Similar results in 1-μm-thick films were obtained by Zhou et al. using a YBCO target added with 5 mol% BZO and 5 mol% Y_2O_3 [199].

More recently, Jha et al. [200, 201] studied systematically the influence of double APCs on the pinning properties of YBCO films grown by PLD on $SrTiO_3$. They used three YBCO-BSO-mixed targets (2 wt% 3wt%, and 4 wt%), fabricating films with each one added with two different areal concentrations of Y_2O_3 (2.2A% and 3A%), and he compared in total ten samples, including YBCO reference and the three samples with BSO only. Both 1D- and 3D-APCs were incorporated in the film according to TEM images (Fig. 2.27a) and are active pinning centers. The

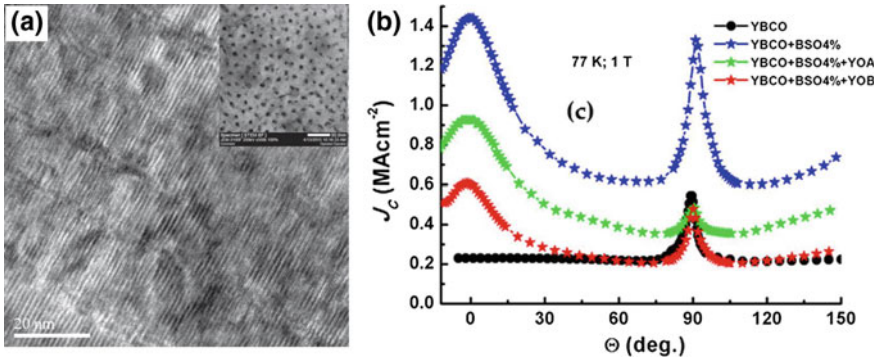

Fig. 2.27 **a** High-resolution TEM image (cross-sectional view) of (**a**) YBCO+BSO 2wt%+Y_2O_3 3A% nanocomposite films. The *inset* shows the planar view of the TEM images; **b** comparison of angular dependence of J_c at 77 K, 1 T for YBCO+BSO 4wt series. (Both figures reproduced with permission from [201])

addition of Y_2O_3 nanoparticles to BSO nanorods improved the F_p^{max}, with shifting of F_p^{max} at higher values of B, due to the increase of pinning center density. Best hybrid sample (YBCO+BSO 3wt%+Y_2O_3 3A%) has $F_p^{max} = 11 GN/m^3$ (77 K, $B//c$). Since this value is lower than in the case of YBCO+BSO 4wt% without Y_2O_3 addition (about 20 GN/m^3), it seems that an excessive concentration of APCs hinders the path of supercurrents.

On the other hand, the addition of Y_2O_3 has the benefit to reduce the anisotropy of J_c in the intermediate region of θ, being θ the angle between the c-axis of the film and the applied magnetic field (Fig. 2.27b).

Horide et al. [202] obtained similar results on IBAD technical substrate with seven YBCO films added with Y_2O_3 and BSO (all the possible combinations of BSO 2wt%, 4wt%, and Y_2O_3 0.69A%, 2.2A%).

In these hybrid YBCO films with nanorods and nanoparticles, when external magnetic field is parallel to c-axis of the film (i.e., parallel to the nanorods), vertical segments of the vortices are strongly pinned by the BSO nanorods and connected by kinks. The contribution from the pinning by continuous nanorods is given by (2.5). This contribution must be combined with the additional contribution from the nanoparticles or from the oxygen vacancies for the pinning of the vortex kink.

The nanoparticles give a contribution which can be expressed by the following equation

$$J_c^{3D-kink} = \frac{\Phi_0}{16\pi\mu_0\lambda_{ab}^2\xi_{ab}}\left[\frac{\xi_c}{l_s}\right] \tag{2.16}$$

where l_s is the length of the kink which corresponds to the spacing between nanorods. The additional oxygen vacancy contribution can be given by

$$J_c^{vac-kink} = \frac{D^2\Phi_0}{64\pi d\mu_0\lambda_{ab}^2\xi_{ab}\xi_c}\sqrt{n\xi_{ab}\xi_c d} \tag{2.17}$$

where $D \approx 20$ nm is the diameter, and $n \approx 10^{26}$ m^{-3} is the concentration of the oxygen vacancies. At $B = 1$ T, $T = 77$ K, the two contributions of the nanodimensional species have been calculated, $J_c^{3D\text{-}kink} = 0.46$ MA/cm^2 and $J_c^{vac\text{-}kink} = 0.28$ MA/cm^2. This difference in J_c values indicates that the vortex pinning for the kinks by the Y_2O_3 nanoparticles is more effective than the one by random point defects provided by oxygen vacancies.

2.3.6.2 Multilayers with Alternate YBCO+1D-APCs and YBCO +3D-APCs Layers

Very recently, Mele et al. [203] tried to add 1D-APCs and 3D-APCs in a separate fashion fabricating 1D+3D multilayers. To this purpose, YBCO+4wt% BSO-mixed target and YBCO+2A% Y_2O_3 surface-modified target were switched in the PLD

chamber, and different configurations of YBCO+BSO layer (nm)/YBCO+Y_2O_3 layer (nm) varied as 90/30, 60/10, and 10/10 were studied.

Overall, it was found that the contribution of 1D pinning is quite superior with respect to that of the 3D ones. Indeed, same as shown in previous sections of the chapter for 1D and 3D cases, the calculated J_c is larger than the measured J_c because of the effect of current blocking by APCs. The general trend $J_c(90/30) > J_c(60/10) > J_c(10/10)$ can be explained in terms of a structural compromise between the APC pinning efficiency and current-blocking effect when the pinning center size is less compatible with other superconducting parameters.

2.3.7 *Combination of APCs Parallel (Nanorods) and Perpendicular (Nanolayers) to C-axis of YBCO Film*

The pinning landscape is enriched by the combination of nanorods parallel to the *c*-axis of the film and nanolayered structures, perpendicular to the *c*-axis. Two cases of hybrid parallel/perpendicular APCs are reported in the literature.

Wee et al. [204] fabricated a hybrid NdBCO film with one half of the film having BZO nanorods aligned along the *c*-axis and the other half of the film having BZO nanoscale defect structures aligned along the *ab* plane. This unique hybrid nanoscale structure resulted in less anisotropy in the angular dependence of J_c compared to pure NdBCO films and to films with nanoscale defects aligned along only one direction.

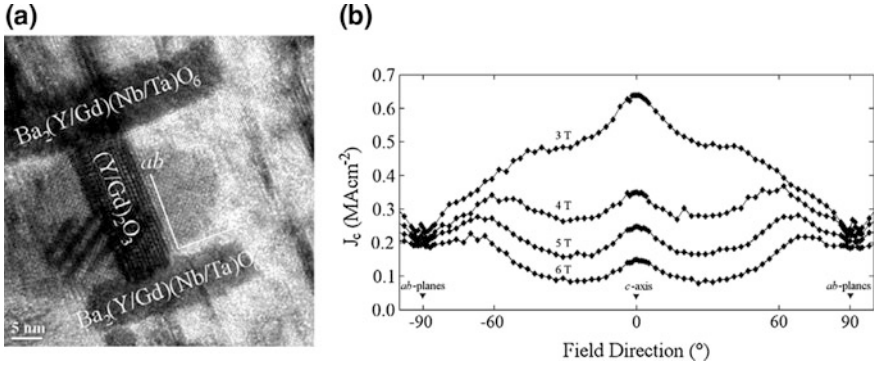

Fig. 2.28 **a** TEM image of the $YBa_2Cu_3O_7$+2.5 mol% Gd_3TaO_7+2.5 mol% Ba_2YNbO_6 sample showing a platelike nanoparticle nucleated between two rod segments (reproduced with permission from [201]); **b** high-field angular dependence of J_c measured at 77 K for a YBCO sample with (Nb–Ta) doping, applied fields ranging from 3 to 6 T. (Reproduced with permission from [206])

In the early work of Ercolano et al. [205], the addition of double perovskite YBa_2NbO_6 generated two kinds of defects: nanorods parallel to the *c*-axis and dispersed nanoparticles, with consequent improvement of pinning in the direction of both *c*-axis (*c*-axis-correlated pinning) and *ab* plane. In an improvement of their previous work [206], Ercolano et al. added Gd_3TaO_7 to Ba_2YNbO_6 in YBCO target and found two kinds of defects in YBCO film after the deposition: $Ba_2(Y/Gd)(Nb/Ta)O_6$ segmented rods and $(Y/Gd)_2O_3$ platelike nanoparticles, parallel and perpendicular to the *c*-axis of the film, respectively (Fig. 2.28a). The two kinds of defects are interconnected, forming a jungle-gym network, and the angular dependence of J_c shows peculiar behavior: Increasing the external magnetic field, isotropic pinning becomes predominant over *c*-axis-correlated pinning (Fig. 2.28b).

2.4 Conclusion

This chapter presents an overview of the last 10-year research on artificial pinning centers (APCs) made by several groups in the world with the purpose of enhancing the performance (critical current and global pinning force) of $YBa_2Cu_3O_y$ (YBCO) thin films and coated conductors.

Impressive results have been achieved and can be summarized as follows

(1) Control of dimensionality and spacing of the APCs have been achieved, and advanced combinations such as segmented nanorods, mixed pinning centers, multilayers, plus nanorods have been incorporated in the YBCO and REBCO films grown on bare, decorated, or buffered crystalline substrates.
(2) The irreversibility field at 77 K was impressively enhanced to over 15 T in optimized SmBCO and GdBCO films and coated conductors added with BHO nanorods without significant depression of the superconducting critical temperature. This enhancement testifies the robustness of REBCO-related films for practical applications.
(3) Outstanding global pinning forces of ~30 GN/m^3 (77 K *B*//*c*), drastically surpassing 15 GN/m^3, the global pinning force of conventional NbTi (4.2 K), have been achieved in short pieces of YBCO added with nanorods ($BaSnO_3$ and niobate) so that the use of liquid nitrogen instead of liquid helium as coolant can be considered for practical applications on the large scale for transformers, fault current limiter (FCL), and cables.
(4) Exemplary performance in conditions of interest for practical applications such as motors, generators, and SMES has been obtained: J_c over 15 MA/cm^2 at 30 K, 3 T in 2.2-μm-thick heavily doped (Gd, Y)$Ba_2Cu_3O_x$ superconductor tapes. Cryocoolers, instead of liquid coolants, are likely to be employed in this *T*/*B* region.
(5) Huge pinning forces have been achieved at low temperatures and ultra-high magnetic fields in YBCO-coated conductors heavily doped with BZO

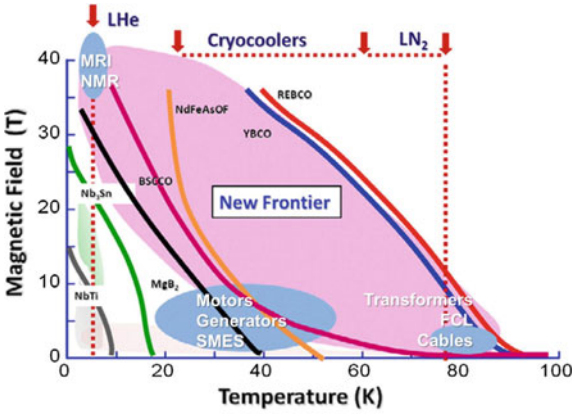

Fig. 2.29 Temperature dependence versus magnetic field diagrams for different superconducting materials including YBCO, REBCO, NdFeAsOF, BSCCO, MgB_2, NbTi, and Nb_3Sn. The new frontier region (40 K–20 T) for the development of applications is indicated together with the three regions where the different power applications and magnets are more likely to occur soon by using coated conductor technology and APCs technology. The temperature regions where the different cryogenic approaches are needed are also indicated. (Reproduced with permission from [43] with slight modification)

nanorods: $F_p^{max} > 1700$ GN/m^3 at 4.2 K, 30 T. Applications such as MRI and NMR are likely to be implemented soon by using HTSC tapes in liquid helium.

The *T*/*B* region described in points (3), (4), and (5) is shown in Fig. 2.29, and new frontier (40 K/20 T) is likely to be approached soon. The incorporation of APCs in YBCO thin films allowed to achieve marvelous performances in a wide range of temperatures (4.2–77 K) and magnetic fields (1–30 T) so that the applicability limit of YBCO+APC thin films and coated conductors was considerably expanded in the past ten years. Remarkable progress in the quality of materials, wide-scale characterization, and large-scale production allows concluding that the future of coated conductors added with APCs for applications on the large scale is bright.

Acknowledgements P.M. recognizes insightful discussions on thin-film deposition, flux pinning, vortex behavior, and APC engineering with many colleagues over the past ten years: K. Matsumoto, Y. Yoshida, S. Awaji, S. Horii, R. Kita, M. Mukaida, A. Ichinose, T. Horide, D. C. Larbalestier, B. Maiorov, V. Selvamanickam, and X. Obradors. P.M. also gratefully thanks H. Abe, H. Honda, S. Saini, A. K. Jha, and S. J. Singh for their invaluable support to the experiments.

P.M. acknowledges partial financial support by Kakenhi S, grant number 23226014.

A.C. acknowledges financial support from Romanian Ministry of Research and Innovation, POC project 28/01.09.2016.

M.I.A. acknowledges partial support from MOHE, Grant Scheme number FRGS/2/2014/SG06/UNITEN/02/3.

References

1. T. Ijima, Oyo Buturi **75**, 26 (2006) (in Japanese)
2. J.L. MacManus Driscoll, S.R. Foltyn, Q.X. Jia, H. Wang, A. Serquis, L. Civale, B. Maiorov, M.E. Hawley, M. Maley, D. E. Peterson, Nat. Mater. **3**, 439 (2004)
3. P. Mele, K. Matsumoto, T. Horide, A. Ichinose, Y. Yoshida, M. Mukaida, S. Horii, R. Kita, Supercond. Sci. Technol. **21**, 032002 (2008)
4. D.M. Feldmann, O. Ugurlu, B. Maiorov, L. Stan, T.G. Holesinger, L. Civale, S.R. Foltyn, Q.X. Jia, Appl. Phys. Lett. **91**, 162501 (2007)
5. S. Miura, Y. Yoshida, Y. Ichino, K. Matsumoto, A. Ichinose, S. Awaji, Supercond. Sci. Technol. **28**, 065013 (2015)
6. V. Selvamanickam, M. Heydari Gharahcheshmeh, A. Xu, Y. Zhang, E. Galstyan, Supercond. Sci. Technol. **28,** 072002 (2015)
7. A. Xu, L. Delgado, N. Khatri, Y. Liu, V. Selvamanickam, D. Abraimov, J. Jarozynski, F. Kametani, D.C. Larbalestier, APL Mater **2**, 046111 (2014)
8. S. Miura, Y. Yoshida, Y. Ichino, A. Tsuruta, K. Matsumoto, A. Ichinose, S. Awaji, Jpn. J. Appl. Phys. **53,** 090304 (2014)
9. S. Awaji, Y. Yoshida, T. Suzuki, K. Watanabe, K. Hikawa, Y. Ichino, T. Izumi, Appl. Phys. Expr. **8**, 023101 (2015)
10. T. Haugan, P.N. Barnes, R. Wheeler, F. Meisenkothen, M. Sumption, Nature **430**, 867 (2004)
11. A. Xu, J. Jarozynski, F. Kametani, D. Larbalestier, Appl. Phys. Lett. **106**, 052603 (2015)
12. M.K. Wu, J.R. Ashburn, C.J. Torng, P.H. Hor, R.L. Meng, Z.J. Huang, Y.Q. Wang, C.W. Chu, Phys. Rev. Lett. **58**, 908 (1987)
13. D. Dimos, P. Chaudhari, J. Mannhart, Phys. Rev. B **41**, 4038 (1990)
14. M. Murakami (ed.), *Melt-processed High-Temperature Superconductors* (World Scientific, Singapore, 1992)
15. M. Tomita, M. Murakami, Nature **421**, 517 (2003)
16. J. Durrell, A. Dennis, J. Jaroszynski, M. Ainslie, K. Plamer, Y. Shi, A. Campbell, J. Hull, M. Strasik, E. Hellstrom, D. Cardwell, Supercond. Sci. Technol. **27**, 082001 (2014)
17. D. Larbalestier, A. Gurevich, D.M. Feldmann, A. Polyanskii, Nature **414**, 368 (2001)
18. M. Parans Paranthaman, T. Izumi (eds.), High-performance YBCO-coated superconductor wires. MRS Bull. **29,** 533–589 (2004)
19. Y. Ijima, K. Onabe, N. Futaki, N. Tanabe, N. Sadakata, O. Kohno, Y. Ikeno, J. Appl. Phys. **74**, 1905 (1993)
20. A. Goyal, D.P. Norton, J.D. Budai, M. Paranthaman, E.D. Specht, D.M. Kroeger, D.K. Christen, Q. He, B. Saffian, F.A. List, D.F. Lee, P.M. Martin, C.E. Klabunde, E. Hartfileld, V.K. Sikka, Appl. Phys. Lett. **69**, 1795 (1996)
21. A. Goyal (ed.), Second-generation HTS conductors (Kluwer Academic Publishers, Dordrecht, 2005)
22. M. Parans Paranthaman, YBa2Cu3O7 coated conductors, *Chapter 4 in "High Temperature Superconductors*", ed. by R. Battacharya, M.P. Paranthaman (Wiley VCH, Weinheim, 2010), pp. 93–101
23. V. Selvamanickam, High temperature superconductor (HTS) wires and tapes, *Chapter 2 in "High Temperature Superconductors (HTS) for Energy*", ed. by Z. Melhem (Woodhead Publishing, Cambridge, 2012), pp. 34–62
24. B. Schey, Pulsed laser deposition of high-temperature superconducting thin films and their applications, *Chapter 14 in "Pulsed Laser Deposition of Thin Films"*, ed. by R. Eason (Wiley, New Jersey, 2007), pp. 313–331
25. M. Miura, Nanostructured oxide superconducting films prepared by metal organic deposition, *Chapter 5 in "Oxide Thin Films, Multilayers, and Nanocomposites"*, ed. by P. Mele, T. Endo, S. Arisawa, C. Li, T. Tsuchiya (Springer, Caham, Heidelberg, 2015), pp. 3–26

26. A. Ignatiev, MOCVD growth of YBCO films for coated conductor applications, *Chapter 15 in "Second-Generation HTS Conductors"*, ed. by A. Goyal (Kluwer Academic Publishers, Dordrecht, 2005), pp. 245–259
27. D.B. Chrisey, G.K. Hubler (eds.), *Pulsed Laser Deposition of Thin Films* (Wiley, New York, 1994), Chapter 8
28. R.K. Singh, D. Kumar, Mat. Sci. Eng. R **22**, 113 (1998)
29. J.M. Hujibregtse, F.C. Klaassen, A. Sziepielow, J.H. Rector, B. Dam, R. Griessen, B.J. Kooi, J.Th.M. De Hosson, Supercond. Sci. Tehnol. **15,** 395 (2002)
30. R.M. Schalk, R. Kundzins, H.W. Weber, E. Stangl, S. Proyer, D. Baüerle, Physica C **257**, 341 (1996)
31. B. Dam, N.J. Koeman, J.H. Rector, B. Stäuble-Pümpin, U. Poppe, R. Griessen, Physica C **261**, 1 (1996)
32. B. Dam, J.M. Hujibregtse, F.C. Klaassen, R.C.F. van der Geest, G. Doornbos, J.H. Rector, A.M. Testa, S. Freisem, J.C. Martinez, B. Stäuble-Pümpin, R. Griessen, Nature **399**, 439 (1999)
33. J.M. Hujibregtse, B. Dam, R.C.F. van der Geest, F.C. Klaassen, R. Elberse, J.H. Rector, R. Griessen, Phys. Rev. B **62**, 1338 (2000)
34. F.C. Klaassen, G. Doornbos, J.M. Hujibregtse, R.C.F. van der Geest, B. Dam, R. Griessen, Phys. Rev. B **64**, 184523 (2001)
35. B. Dam, J.M. Hujibregtse, J.H. Rector, Phys. Rev. B **65**, 064528 (2002)
36. V. Pan, Y. Cherpak, V. Komashko, S. Pozigun, C. Tretiachenko, A. Semenov, E. Pashitskii, A.V. Pan, Phys. Rev. B **73**, 054508 (2006)
37. J. Wang, J.H. Kwon, J. Yoon, H. Wang, T.J. Haughan, F.J. Baca, N.A. Pierce, P.N. Barnes, Appl. Phys. Lett. **92**, 082507 (2008)
38. S. Foltyn, L. Civale, J.L. Macmanus-Driscoll, Q.X. Jia, B. Maiorov, H. Wang, M. Maley, Nat. Mater. **6**, 631 (2007)
39. S.H. Wee, A. Goyal, P.M. Martin, L. Heatherley, Supercond. Sci. Tech. **19**, 865 (2006)
40. Y. Yoshida, K. Matsumoto, Y. Ichino, M. Itoh, A. Ichinose, S. Horii, M. Mukaida, Y. Takai, Jpn. J. Appl. Phys. **44**, L129 (2005)
41. D.R. Nelson, V.M. Vinokur, Phys. Rev. B **48**, 13060 (1993)
42. G. Blatter, M.V. Feigel`man, V.B. Genskenbein, A.I. Larkin, V.M. Vinokur, Rev. Mod. Phys. **86,** 1125 (1994)
43. X. Obradors, T. Puig, Supercond. Sci. Technol. **27**, 044003 (2014)
44. T.J. Haugan, T.A. Campbell, N.A. Pierce, M.F. Locke, I. Maartense, P.N. Barnes, Supercond. Sci. Technol. **21**, 012503 (2008)
45. P.N. Barnes, J.W. Kell, B.C. Harrison, T.J. Haugan, C.V. Varanasi, M. Rane, F. Ramos, Appl. Phys. Lett. **89**, 0122503 (2006)
46. H. Zhou, B. Maiorov, H. Wang, J.L. MacManus-Driscoll, T.G. Holesinger, L. Civale, Q.X. Jia, S.R. Foltyn, Supercond. Sci. Technol. **21**, 025001 (2008)
47. A. Radhika Devi, V. Seshu Bai, P.V. Patanjali, R. Pinto, N. Harish Kumar, S.K. Malik, Supercond. Sci. Technol. **13**, 935 (2000)
48. S. Horii, A. Ichinose, Y. Ichino, T. Ozaki, Y. Yoshida, K. Matsumoto, M. Mukaida, J. Shimoyama, K. Kishio, Physica C **463–465**, 922 (2007)
49. M. Muralidhar, N. Sakai, M. Jirsa, M. Murakami, I. Hirabayashi, Appl. Phys. Lett. **92**, 162512 (2008)
50. M. Muralidhar, N. Sakai, T. Nishiyama, M. Jirsa, T. Machi, M. Murakami, Appl. Phys. Lett. **82**, 943 (2003)
51. M. Muralidhar, N. Sakai, M. Jirsa, N. Koshizuka, M. Murakami, Appl. Phys. Lett. **83**, 5005 (2003)
52. C. Cai, B. Holzapfel, J. Hänisch, L. Fernández, L. Schultz, Applied. Phys. Lett. **84**, 0377 (2004)
53. C. Cai, B. Holzapfel, J. Hänisch, L. Fernández, L. Schultz, Phys. Rev. B **69**, 104531 (2004)
54. R.-K. Ko, S.-H. Bae, M.-J. Jung, S.-H. Jang, K.-J. Song, C. Park, M.-H. Sohn, S.-I. Kang, S.-S. Oh, D.-W. Ha, H.-S. Kim, Y.-C. Kim, I.E.E.E. Trans, Appl. Superc. **19**, 3136 (2009)

55. L. Civale, A.D. Marwick, T.K. Worthington, M.K. Kirk, J.R. Thompson, L. Krusin-Elbaum, Y. Sun, J.R. Clem, F. Holtzberg, Phys. Rev. Lett. **67**, 648 (1991)
56. L. Civale, Supercond. Sci. Technol. **10**, A11 (1997)
57. B. Holzapfel, G. Kreiselmeyer, M. Kraus, G. Saemann-Ishenko, S. Bouffard, S. Klaumünzer, L. Schultz, Phys. Rev. B **48**, 600 (1993)
58. L.M. Paulius, J.A. Fendrich, W.-K. Kwok, A.E. Koshelev, V.M. Vinokur, G.W. Crabtree, B.G. Glagola, Phys. Rev. B **56**, 913 (1997)
59. N. Chikumoto, Enhancement of flux pinning through irradiation, *Chapter 6 in "Critical Currents in Superconductors"*, ed. by T. Takizawa, M. Murakami (Fuzambo International, 2005), pp. 91–103
60. Q. Li, *Presented at CCA2014*, Jeju, South Korea, 2 Dec 2014
61. M. Leroux, K.J. Kihlstrom, S. Holleis, M.W. Rupich, S. Sathyamurthy, S. Fleshler, H. Sheng, D.J. Miller, S. Eley, L. Civale, A. Kayani, P.M. Niraula, U. Welp, W.-K. Kwok, Appl. Phys. Lett. **107**, 192601 (2015)
62. K. Develos-Bagarinao, S.C. Wimbush, H. Matsui, I. Yamaguchi, J.L. MacManus-Driscoll, Supercond. Sci. Technol. **25**, 065005 (2012)
63. T. Sueyoshi, Y. Furuki, T. Kai, T. Fujiyoshi, N. Ishikawa, Physica C **504**, 53 (2014)
64. A. Crisan, S. Fujiwara, J.C. Nie, A. Sundaresan, H. Ihara, App. Phys. Lett. **79**, 4547 (2001)
65. A. Crisan, P. Badica, S. Fujiwara, J.C. Nie, A. Sundaresan, Y. Tanaka, H. Ihara, App. Phys. Lett. **80**, 3566 (2002)
66. A. Crisan, P. Badica, S. Fujiwara, J.C. Nie, A. Sundaresan, A. Iyo, Y. Tanaka, I.E.E.E. Trans, Appl. Supercond. **13**, 3726 (2003)
67. J.C. Nie, H. Yamasaki, H. Yamada, Y. Nakagawa, K. Develos-Bagarinao, Y. Mawatari, Supercond. Sci. Tech. **17**, 845 (2004)
68. X.M. Cui, G.Q. Liu, J. Wang, Z.C. Huang, Y.T. Zhao, B.W. Tao, Y.R. Li, Physica C **466**, 1 (2007)
69. T. Aytug, M. Paranthaman, A.A. Gapud, S. Kang, H.M. Christen, K.J. Leonard, P.M. Martin, J.R. Thompson, D.K. Christen, R. Meng, I. Rusakova, C.W. Chu, T.H. Johansen, J. Appl. Phys. **98**, 114309 (2005)
70. P. Mikheenko, A. Sarkar, V.-S. Dang, J.L. Tanner, J.S. Abell, A. Crisan, Physica C **469**, 798 (2009)
71. A. Sarkar, P. Mikheenko, V.-S. Dang, J.S. Abell, A. Crisan, Physica C **469**, 1550 (2009)
72. T. Aytug, M. Paranthaman, K.J. Leonard, K. Kim, A.O. Ijadoula, Y. Zhang, E. Tuncer, J.R. Thompson, D.K. Christen, J. Appl. Phys. **104**, 043906 (2008)
73. M. Sparing, E. Backen, T. Freudenberg, R. Hühne, B. Rellinghaus, L. Schultz, B. Holzapfel, Supercond. Sci. Tech. **20**, S239 (2007)
74. F.J. Baca, D. Fisher, R.L.S. Emergo, J.Z. Wu, Supercond. Sci. Technol. **20**, 554 (2007)
75. K. Matsumoto, T. Horide, K. Osamura, M. Mukaida, Y. Yoshida, A. Ichinose, S. Horii, Physica C **412–414**, 1267 (2004)
76. K. Matsumoto, T. Horide, P. Mele, A. Ichinose, S. Horii, Y. Yoshida, M. Mukaida, K. Osamura, IEEE Trans. Appl. Supercond. **13,** 3374 (2003)
77. K. Matsumoto, T. Horide, P. Mele, Y. Yoshida, M. Mukaida, A. Ichinose, S. Horii, Physica C **426–431**, 1091 (2005)
78. K. Matsumoto, T. Horide, A. Ichinose, S. Horii, Y. Yoshida, M. Mukaida, Jpn. J. Appl. Phys. **7**, L246 (2005)
79. P. Mele, K. Matsumoto, T. Horide, O. Miura, A. Ichinose, M. Mukaida, Y. Yoshida, S. Horii, Physica C **648**, 445–448 (2006)
80. P. Mele, K. Matsumoto, T. Horide, O. Miura, A. Ichinose, M. Mukaida, Y. Yoshida, S. Horii, Supercond. Sci. Technol. **19**, 44 (2006)
81. Y. Yoshida, K. Matsumoto, M. Miura, Y. Ichino, Y. Takai, A. Ichinose, S. Horii, M. Mukaida, Jpn. J. Appl. Phys. **18**, L546 (2005)
82. C.-F. Tsai, J. Huang, J.-H. Lee, F. Khatkhatay, L. Chen, A. Chen, Q. Su, H. Wang, Physica C **510**, 13 (2015)

83. T. Horide, K. Taguchi, K. Matsumoto, N. Matsukida, M. Ishimaru, P. Mele, R. Kita, Appl. Phys. Let. **108**, 082601 (2016)
84. A. Goyal, S. Kang, K.J. Leonard, P.M. Martin, A.A. Gapud, M. Varela, M. Paranthaman, A.O. Ijaduola, E.D. Specht, J.R. Thompson, D.K. Christen, S.J. Pennycook, F.A. List, Supercond. Sci. Technol. **18**, 1533 (2005)
85. Y. Yamada, K. Takahashi, H. Kobayashi, M. Konishi, T. Watanabe, A. Ibi, T. Muroga, S. Miyata, T. Kato, T. Hirayama, Y. Shiohara, Appl. Phys. Lett. **87**, 132502 (2005)
86. P. Mele, K. Matsumoto, T. Horide, A. Ichinose, M. Mukaida, Y. Yoshida. S. Horii, Supercond. Sci. Technol. **20,** 244 (2007)
87. S. Kang, A. Goyal, J. Li, A.A. Gapud, P.M. Martin, L. Heatherly, J.R. Thompson, D.K. Christen, F.A. List, M. Paranthaman, D.F. Lee, Science **311**, 1911 (2006)
88. A. Ichinose, K. Naoe, T. Horide, K. Matsumoto, R. Kita, M. Mukaida, Y. Yoshida, S. Horii, Supercond. Sci. Technol. **20**, 1144 (2007)
89. S. Kang, A. Goyal, J. Li, P. Martin, A. Ijaduola, J.R. Thompson, M. Paranthaman, Physica C **457**, 41 (2007)
90. M. Inoue, T. Kiss, K. Motoyama, T. Nakamura, T. Fujiwara, D. Mitsui, S. Awaji, K. Watanabe, A. Ibi, K. Takahashi, S. Miyata, Y. Yamada, Y. Shiohara, Physica C **463–465**, 674 (2007)
91. K.J. Song, R.K. Ko, Y.S. Lee, J.S. Yang, Y.M. Park, M. Dixit, H.S. Kim, H.S. Ha, D.W. Ha, S.S. Oh, D.J. Kim, C. Park, S.I. Yoo, Physica C **445–448**, 656 (2006)
92. P. Paturi, M. Irjala, H. Huhtinen, J. Appl. Phys. **103,** 123907 (2008)
93. M. Peurla, H. Huhtinen, M.A. Shakhov, K. Traito, Yu.P. Stepanov, M. Safonchik, P. Paturi, Y. Y. Tse, R. Palai, R. Laiho, Phys. Rev. B **75,** 184524 (2007)
94. M. Peurla, P. Paturi, Yu.P. Stepanov, H. Huhtinen, Y.Y. Tse, A.C. Bódi, J. Raittila, R. Laiho, Supercond. Sci. Technol. **19,** 767 (2006)
95. P. Paturi, M. Irjala, H. Huhtinen, A.B. Abrahamsen, J. Appl. Phys. **105,** 23904 (2009)
96. M. Safonchik, K. Traito, S. Tuominen, P. Paturi, H. Huhtinen, R. Laiho, Supercond. Sci. Technol. **22**, 065006 (2009)
97. K. Traito, M. Peurla, H. Huhtinen, Yu.P. Stepanov, M. Safonchik, Y.Y. Tse, P. Paturi, R. Laiho, Phys. Rev. B **73,** 224522 (2006)
98. F.J. Baca, P.N. Barnes, R.L.S. Emergo, T.J. Haugan, J.N. Reichart, J.Z. Wu, Appl. Phys. Lett. **94**, 102512 (2009)
99. S.H. Wee, A. Goyal, Y.L. Zuev, C. Cantoni, Supercond. Sci. Technol. **21**, 092001 (2008)
100. B. Maiorov, S.A. Baily, H. Zhou, O. Ugurlu, J.A. Kennison, P.C. Dowden, T.G. Holesinger, S.R. Foltyn, L. Civale, Nat. Mater. **8**, 398 (2009)
101. S.H. Wee, A. Goyal, J. Li, Y.L. Zuev, S. Cook, L. Heatherly, Supercond. Sci. Technol. **20**, 789 (2007)
102. S.H. Wee, A. Goyal, J. Li, Y.L. Zuev, S. Cook, J. Appl. Phys. **102**, 063906 (2007)
103. Y.L. Zuev, D.K. Christen, S.H. Wee, A. Goyal, S.W. Cook, Appl. Phys. Lett. **93**, 172512 (2008)
104. S.H. Wee, A. Goyal, P.M. Martin, J. Li, M. Paranthaman, L. Heatherly, Supercond. Sci. Technol. **19**, L42 (2006)
105. M. Mukaida, T. Horide, R. Kita, S. Horii, A. Ichinose, Y. Yoshida, O. Miura, K. Matsumoto, K. Yamada, N. Mori, Jpn. J. Appl. Phys. **44**, L952 (2005)
106. M. Ito, M. Mukaida, T. Ohazama, R. Kita, A. Ichinose, S. Horii, A. Saito, K. Matsumoto, Y. Yoshida, K. Koike, F. Hirose, S. Ohshima, Physica C **426–431**, 1415 (2005)
107. M. Haruta, T. Fujiyoshi, T. Sueyoshi, K. Dezaki, D. Ichigosaki, K. Miyahara, R. Miyagawa, M. Mukaida, K. Matsumoto, Y. Yoshida, A. Ichinose, S. Horii, Supercond. Sci. Technol. **19**, 803 (2006)
108. T. Fujiyoshi, M. Haruta, T. Sueyoshi, K. Yonekura, M. Watanabe, M. Mukaida, R. Teranishi, K. Matsumoto, Y. Yoshida, A. Ichinose, S. Horii, S. Awaji, K. Watanabe, Physica C **468**, 1635 (2008)
109. M. Miura, M. Mukaida, K. Matsumoto, Y. Yoshida, A. Ichinose, S. Horii, R. Kita, A. Saito, K. Kaneko, K. Yamada, N. Mori, Physica C **445–448**, 845 (2006)

110. Y. Yoshida, T. Ozaki, Y. Ichino, Y. Takai, K. Matsumoto, A. Ichinose, M. Mukaida, S. Horii, Physica C **468**, 1606 (2008)
111. V. Selvamanickam, M. Heydari Gharahcheshmeh, A. Xu, E. Galstyan, L. Delgado, C. Cantoni, Appl. Phys. Lett. **106**, 032601 (2015)
112. A. Xu, L. Delgado, M. Heydari Gharahcheshmeh, N. Kahtri, Y. Liu, V. Selvamanickam, Supercond. Sci. Technol. **28,** 082001 (2015)
113. V. Selvamanickam, M. Heydari Gharahcheshmeh, A. Xu, Y. Zhang, E. Galstyan, Supercond. Sci. Technol. **28,** 104003 (2015)
114. Ch.V. Varanasi, P.N. Barnes, J. Burke, L. Brunke, I. Maartense, T.J. Haugan, E.A. Stinzianni, K.A. Dunn, P. Haldar, Supercond. Sci. Technol. **19**, L37 (2006)
115. C.V. Varanasi, J. Burke, L. Brunke, H. Wang, M. Sumption, P.N. Barnes, J. Appl. Phys **102**, 063909 (2007)
116. C.V. Varanasi, J. Burke, L. Brunke, H. Wang, J.H. Lee. P.N. Barnes, J. Mater. Res. **23,** 3363 (2008)
117. P. Mele, K. Matsumoto, T. Horide, A. Ichinose, M. Mukaida, Y. Yoshida. S. Horii, R. Kita, Supercond. Sci. Technol. **21,** 125017 (2008)
118. C.V. Varanasi, J. Burke, H. Wang, J.H. Lee, P.N. Barnes, Appl. Phys. Lett. **93**, 092501 (2008)
119. M. Namba, S. Awaji, K. Watanabe, S. Ito, E. Aoyagi, H. Kai, M. Mukaida, R. Kita, Appl. Phys. Express **2**, 073001 (2009)
120. S. Yasunaga, M. Mukaida, A. Ichinose, S. Horii, R. Teranishi, K. Yamada, K. Matsumoto, R. Kita, Y. Yoshida, N. Mori, Physica C **468**, 1858 (2008)
121. Y. Tanaka, M. Mukaida, R. Teranishi, K. Yamada, A. Ichinose, K. Matsumoto, S. Horii, Y. Yoshida, R. Kita, T. Fujiyosh, N. Mori, Physica C **468**, 1864 (2008)
122. L. Civale, B. Maiorov, A. Serquis, J.O. Willis, J.Y. Coulter, H. Wang, Q.X. Jia, P.N. Arendt, J.L. MacManus-Driscoll, M.P. Maley, S.R. Foltyn, Appl. Phys. Lett. **84**, 2121 (2004)
123. H. Tobita, K. Notoh, K. Higashikawa, M. Inoue, T. Kiss, T. Kato, T. Hirayama, M. Yoshizumi, T. Izumi, Y. Shiohara, Supercond. Sci. Technol. **25**, 062002 (2012)
124. A. Tsuruta, Y. Yoshida, Y. Ichino, A. Ichinose, K. Matsumoto, S. Awaji, J. Appl. Phys. **52**, 010201 (2013)
125. A. Tsuruta, Y. Yoshida, Y. Ichino, A. Ichinose, K. Matsumoto, S. Awaji, Supercond. Sci. Technol. **27**, 065001 (2014)
126. A. Tsuruta, Y. Yoshida, Y. Ichino, A. Ichinose, S. Watanabe, T. Horide, K. Matsumoto, S. Awaji, Appl. Phys. Expr. **8**, 033101 (2015)
127. S.A. Harrington, J.H. Durrell, B. Maiorov, H. Wang, S.C. Wimbush, A. Kursumovic, J.H. Lee, J.L. MacManus-Driscoll, Supercond. Sci. Technol. **22**, 022001 (2009)
128. D.M. Feldmann, T.G. Holesinger, B. Maiorov, S.R. Foltyn, J.Y. Coulter, I. Apodaca, Supercond. Sci. Technol. **23**, 095004 (2010)
129. J.J. Shi, J.Z. Wu, Phil. Mag. **92**, 2911 (2012)
130. J.J. Shi, J.Z. Wu, Phil. Mag. **92**, 4205 (2012)
131. F.J. Baca, T.J. Haugan, P.N. Barnes, T.G. Holesinger, B. Maiorov, R. Lu, X. Wang, J.N. Reichart, J.Z. Wu, Adv. Funct. Mater. **23**, 4826 (2013)
132. J.Z. Wu, J.J. Shi, J.F. Baca, R. Emergo, T.J. Haugan, B. Maiorov, T. Holesinger, Supercond. Sci. Technol. **27**, 044010 (2014)
133. J. Wu, Three-dimensional pinning landscape based on orientation phase diagram of BaZrO3 nanostructures in YBa2Cu3O7 films, in *Presented at IUMRS-ICA 2014*, Fukuoka, Japan, C9-I25-007
134. J.J. Shi, J.Z. Wu, J. Appl. Phys. **118**, 164301 (2015)
135. S.R. Foltyn, P. Tiwari, R.C. Dye, M.Q. Le, X.D. Wu, Appl. Phys. Lett. **63**, 1848 (1993)
136. S.R. Foltyn, Q.X. Jia, P.N. Arendt, L. Kinder, Y. Fan, J.F. Smith, Appl. Phys. Lett. **75**, 3692 (1999)
137. S.R. Foltyn, P.N. Arendt, Q.X. Jia, H. Wang, J.L. MacManus-Driscoll, S. Kreiskott, R.F. DePaula, L. Stan, J.R. Groves, P.C. Dowden, Appl. Phys. Lett. **82**, 4519 (2003)

138. A.O. Ijaduola, J.R. Thompson, R. Feenstra, D.K. Christen, A.A. Gapud, X. Song, Phys. Rev. B **73**, 134502 (2006)
139. S.I. Kim, A. Gurevich, X. Song, X. Li, W. Zhang, T. Kodenkandath, M.W. Rupich, T.G. Holesinger, D.C. Larbalestier, Supercond. Sci. Technol. **19**, 968 (2006)
140. Z.J. Chen, D.M. Feldmann, D.C. Larbalestier, T.G. Holesinger, X. Li, W. Zhang, M.W. Rupich, Appl. Phys. Lett. **91,** 052508 (2007)
141. Yu.V. Cherpak, V.O. Moskaliuk, A.V. Semenov, V.L. Svetchnikov, C.G. Tretiatchenko,V. M. Pan, Supercond. Sci. Technol. **20,** 1159 (2007)
142. Z. Chen, F. Kametani, S.I. Kim, D.C. Larbalestier, H.W. Jang, K.J. Choi, C.B. Eom, J. Appl. Phys. **108**, 043913 (2008)
143. S.R. Foltyn, H. Wang, L. Civale, Q.X. Jia, P.N. Arendt, B. Maiorov, Y. Li, M.P. Maley, J. MacManus-Driscoll, Appl. Phys. Lett. **87**, 162505 (2005)
144. A.A. Gapud, D. Kumar, S.K. Viswanathan, C. Cantoni, M. Varela, J. Abiade, S.J. Pennycook, D.K. Christen, Supercond. Sci. Technol. **18**, 1502 (2005)
145. C.B. Cai, J.C. Zhang, S.X. Cao, J. Hänisch, R. Hühne, B. Holzapfel, Physica C **460–462**, 1355 (2007)
146. K. Develos-Bagarinao, H. Yamasaki, K. Ohki, Y. Nakagawa, Supercond. Sci. Technol. **20**, L25 (2007)
147. K. Develos-Bagarinao, H. Yamasaki, K. Ohki, J. Appl. Phys. **104**, 063907 (2008)
148. T.G. Holesinger, Q. Jia, B. Maiorov, L. Civale, P.C. Dowden, B.J. Gibbons, Adv. Mater. **19**, 1917 (2007)
149. A.V. Pan, S. Pysarenko, S.X. Dou, Appl. Phys. Lett. **98**, 232506 (2006)
150. T. Haugan, P.N. Barnes, I. Maartense, C.B. Cobb, E.J. Lee, M. Sumption, J. Mater. Res. **18**, 2618 (2003)
151. L. Peng, C. Cai, C. Chen, Z. Liu, R. Hühne, B. Holzapfel, J. Appl. Phys. **104**, 033920 (2008)
152. C. Cai, J. Liu, Z. Liu, L. Ying, B. Gao, L. Peng, C. Chen, J. Appl. Phys. **104**, 023913 (2008)
153. S. Kang, K.J. Leonard, P.M. Martin, J. Li, A. Goyal, Supercond. Sci. Technol. **20**, 11 (2007)
154. H. Huhtinen, K. Schlesier, P. Paturi, Supercond. Sci. Technol. **22**, 075019 (2009)
155. P.K. Petrov, Z.G. Ivanov, S.S. Gevorgyan, Mat. Sci. Eng. B **A288**, 231 (2000)
156. W.S. Tan, H.L. Cai, J.S. Liu, X.S. Wu, S.S. Jiang, Z.H. Wu, Q.J. Jia, J. Gao, J. Appl. Phys. **99**, 08M509 (2006)
157. T. Sueyoshi, M. Watanabe, M. Haruta, T. Fujiyoshi, K. Miyahara, T. Ikegami, K. Ebihara, R. Miyagawa, Physica C **468**, 1266 (2008)
158. T. Ozaki, Y. Yoshida, M. Miura, Y. Ichino, Y. Takai, K. Matsumoto, A. Ichinose, S. Horii, M. Mukaida, Physica C **463–465**, 649 (2007)
159. S. Horii, M. Takamura, M. Mukaida, A. Ichinose, K. Yamada, R. Teranishi, K. Matsumoto, R. Kita, Y. Yoshida, J. Shimoyama, K. Kishio, Appl. Phys. Lett. **92**, 132502 (2008)
160. M. Mukaida, S. Miyazawa, Appl. Phys. Lett. **63**, 999 (1993)
161. M. Takamura, M. Mukaida, Y. Shingai, R. Teranishi, K. Yamada, N. Mori, S. Horii, A. Ichinose, R. Kita, S. Kato, K. Matsumoto, Y. Yoshida, Physica C **463–465**, 904 (2007)
162. M. Takamura, M. Mukaida, S. Horii, A. Ichinose, R. Kita, S. Kato, K. Matsumoto, Y. Yoshida, M. Namba, S. Awaji, K. Watanabe, T. Fujiyoshi, R. Teranishi, K. Yamada, N. Mori, Physica C **468**, 1851 (2008)
163. K. Matsumoto, D. Takahara, T. Horide, A. Ichinose, S. Horii, Y. Yoshida, M. Mukaida, K. Osamura, IEEE Trans. Appl. Supercond. **15,** 2719 (2005)
164. P. Mikheenko, V.S. Dang, Y.Y. Tse, M.M. Awang Kechik, P. Paturi, H. Huhtinen, Y. Wang, A. Sarkar, J.S. Abell, A. Crisan, Supercond. Sci. Technol. **23,** 125007 (2010)
165. P. Mikheenko, V.S. Dang, M.M. Awang Kechik, A. Sarkar, P. Paturi, H. Huhtinen, J.S. Abell, A. Crisan, IEEE Trans. Appl. Supercond. **21,** 3184 (2011)
166. A. Crisan, V.S. Dang, G. Yearwood, P. Mikheenko, H. Huhtinen, P. Paturi, Physica C **503**, 89 (2014)
167. M. Miura, T. Kato, M. Yoshizumi, Y. Yamada, T. Izumi, Y. Shiohara, T. Hirayama, Appl. Phys. Express **1**, 051701 (2008)

168. J. Gutiérrez, A. Llordes, J. Gázquez, M. Gibert, N. Romà, S. Ricart, A. Pomar, F. Sandiumenge, N. Mestres, T. Puig, X. Obradors, Nat. Mater. **6**, 367 (2007)
169. A. Lordes, A. Palau, J. Gazquez, M. Coll, R. Vlad, A. Pomar, J. Arbiol, R. Guzman, S. Ye, V. Ruoco, F. Sandiumenge, S. Ricart, T. Puig, M. Varela, D. Chateigner, J. Vanacken, J. Gutierrez, V. Moschalkov, G. Deutscher, C. Magen, X. Obradors, Nat. Mater. **11**, 329 (2012)
170. Y. Yoshida, K. Matsumoto, Y. Ichino, M. Itoh, A. Ichinose, S. Horii, M. Mukaida, Y. Takai, Jpn. J. Appl. Phys. **44**, L129 (2005)
171. Y. Yoshida, Y. Ichino, M. Miura, Y. Takai, K. Matsumoto, A. Ichinose, S. Horii, M. Mukaida, IEEE Trans. Appl. Supercond. **15**, 2727 (2005)
172. M. Miura, Y. Yoshida, Y. Ichino, Y. Takai, K. Matsumoto, A. Ichinose, S. Horii, M. Mukaida, Jpn. J. Appl. Phys. **45**, L11 (2006)
173. Y. Ichino, Y. Yoshida, M. Miura, Y. Takai, K. Matsumoto, M. Mukaida, A. Ichinose, S. Horii, S. Awaji, K. Watanabe, Physica C **463–465**, 639 (2007)
174. Y. Yoshida, Y. Ichino, M. Miura, T. Ozaki, Y. Takai, K. Matsumoto, A. Ichinose, M. Mukaida, S. Horii, Physica C **463–465**, 633 (2007)
175. R.L.S. Emergo, J.Z. Wu, T.J. Haugan, P.N. Barnes, Appl. Phys. Lett. **87**, 232503 (2005)
176. C. Varanasi, P.N. Barnes, J. Burke, J. Carpenter, T.J. Haugan, Appl. Phys. Lett. **87**, 262510 (2005)
177. M.D. Sumption, T.J. Haugan, P.N. Barnes, T.A. Campbell, N.A. Pierce, C. Varanasi, Phys. Rev. B **77**, 094506 (2008)
178. S.I. Kim, F. Kametani, Z. Chen, A. Gurevich, D.C. Larbalestier, T. Haugan, P. Barnes, Appl. Phys. Lett. **90**, 252502 (2007)
179. T.A. Campbell, T.J. Haugan, I. Maartense, J. Murphy, L. Brunke, P.N. Barnes, Physica C **423**, 1 (2005)
180. V.F. Solovyov, H.J. Wiesmann, L. Wu., Q. Li., L.D. Cooley, M. Suenaga, B. Maiorov, L. Civale, Supercond. Sci. Technol. **20,** L20 (2007)
181. H. Yamasaki, K. Ohki, H. Yamada, Y. Nakagawa, Y. Mawatari, Supercond. Sci. Technol. **21**, 125011 (2008)
182. S.K. Viswanathan, A.A. Gapud, M. Varela, J.T. Abiade, D.K. Christen, S.J. Pennycook, D. Kumar, Thin Solid Films **515**, 6452 (2007)
183. J. Hänisch, C. Cai, R. Hühne, L. Schultz, B. Holzapfel, Appl. Phys. Lett. **86**, 122508 (2005)
184. S. Engel, T. Thersleff, R. Hühne, L. Schultz, B. Holzapfel, Appl. Phys. Lett. **90**, 102505 (2007)
185. R. Kalyanaraman, S. Oktyabrsky, J. Narayan, J. Appl. Phys. **85**, 6636 (1999)
186. T. Horide, K. Matsumoto, H. Adachi, D. Takahara, K. Osamura, A. Ichinose, M. Mukaida, Y. Yoshida, S. Horii, Physica C **445–448**, 652 (2006)
187. M.M. Awang Kechik, P. Mikheenko, A. Sarkar, V.S. Dang, N. Hari Babu, D.A. Cardwell, J.S. Abell, A. Crisan, Supercond. Sci. Technol. **22,** 034020 (2009)
188. P. Mele, K. Matsumoto, T. Horide, A. Ichinose, M. Mukaida, Y. Yoshida. S. Horii, Supercond. Sci. Technol. **20,** 616 (2007)
189. P. Mele, R. Guzman, J. Gazquez, X. Obradors, T. Puig, S. Saini, Y. Yoshida, M. Mukaida, A. Ichinose, K. Matsumoto, M.I. Adam, Supercond. Sci. Technol. **28**, 024002 (2015)
190. C. Meingast, D.C. Larbalestier, J. Appl. Phys. **66**, 5971 (1989)
191. A. Gurevich, Supercond. Sci. Technol. **20**, S128 (2007)
192. E.H. Brandt, Phys. Rev. Lett. **69**, 1105 (1992)
193. A.E. Koshelev, A.B. Kolton, Phys. Rev. B **84**, 104528 (2011)
194. T. Horide, K. Matsumoto, P. Mele, Y. Yoshida, A. Ichinose, R. Kita, S. Horii, M. Mukaida, Phys. Rev. B **79**, 092504 (2009)
195. K. Matsumoto, I. Tanaka, T. Horide, P. Mele, Y. Yoshida, S. Awaji, J. Appl. Phys. **116**, 163903 (2014)
196. K. Matsumoto, T. Horide, A.K. Jha, P. Mele, Y. Yoshida, S. Awaji, IEEE Trans. Appl. Supercond. **25,** 800106 (2015)

197. T. Horide, T. Murayama, K. Takata, K. Matsumoto, P. Mele, Y. Yoshida, Y. Ichino, S. Awaji, J. Appl. Phys. **114**, 073903 (2013)
198. P. Mele, K. Matsumoto, T. Horide, A. Ichinose, M. Mukaida, Y. Yoshida. S. Horii, Supercond. Sci. Technol. **21**, 015019 (2008)
199. H. Zhou, B. Maiorov, S.A. Baily, P.C. Dowden, J.A. Kennison, L. Stan, T.G. Holesinger, Q.X. Jia, S.R. Foltyn, L. Civale, Supercond. Sci. Technol. **22**, 085013 (2009)
200. A.K. Jha, K. Matsumoto, T. Horide, S. Saini, P. Mele, Y. Yoshida, S. Awaji, I.E.E.E. Trans, Appl. Supercond. **25**, 8000505 (2015)
201. A.K. Jha, K. Matsumoto, T. Horide, S. Saini, P. Mele, A. Ichinose, Y. Yoshida, S. Awaji, Supercond. Sci. Technol. **28**, 114004 (2015)
202. T. Horide, T. Kawamura, K. Matsumoto, A. Ichinose, M. Yoshizumi, T. Izumi, Y. Shiohara, Supercond. Sci. Technol. **26**, 075019 (2013)
203. P. Mele, M.I. Adam, T. Suzuki, Y. Yoshida, S. Awaji, A. Ichinose, S. Saini, A.K. Jha, K. Matsumoto, Sci. Adv. Mater. **9**, 1042 (2017)
204. S.H. Wee, A. Goyal, Y.L. Zuev, C. Cantoni, Appl. Phys. Express **1**, 111702 (2009)
205. G. Ercolano, S.A. Harrington, H. Wang, C.F. Tsai, J.L. MacManus-Driscoll, Supercond. Sci. Technol. **23**, 022003 (2010)
206. G. Ercolano, M. Bianchetti, S.C. Wimbush, S.A. Harrington, H. Wang, J.H. lee, J.L. MacManus-Driscoll, Supercond. Sci. Technol. **24**, 095012 (2011)

http://www.springer.com/978-3-319-59353-1

Vortices and Nanostructured Superconductors
Crisan, A. (Ed.)
2017, XIV, 259 p. 121 illus., 63 illus. in color., Hardcover
ISBN: 978-3-319-59353-1